UNIVERSITÀ DEGLI STUDI DI CATANIA
FACOLTÀ DI INGEGNERIA

Dottorato di Ricerca in Ingegneria Elettronica, Automatica e del Controllo dei Sistemi Complessi
XXIV CICLO

Tesi di Dottorato

AGNESE DI STEFANO

Next generation of numerical models for inferring the volcano dynamics from geophysical observations

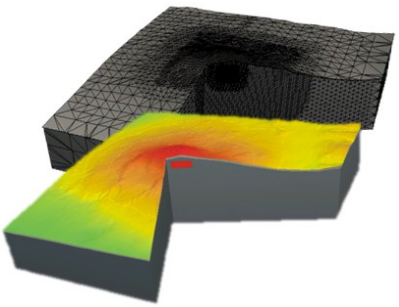

Tutors: Prof. Eng. Luigi Fortuna
Dr. Ciro Del Negro
Eng. Gilda Currenti

Coordinator: Prof. Eng. Luigi Fortuna

to my aunty Melina

Acknowledgements

A sincere thank goes to my tutor and Ph.D. school coordinator Prof. Eng. Luigi Fortuna who, first, gave me the possibility to have this experience and always represented a reference point in my scientific path.

I would like to express my gratitude to my tutor Dr. Ciro Del Negro for supervising my work and for offering his expertise to make me develop my knowledge about Volcano Geophysics.

I am grateful to the members of the the research groups of the the "Unità Funzionale Gravimetria e Magnetismo" at "Istituto Nazionale di Geofisica e Vulcanologia" for their support and patience. Especially I'd like to thank Eng. Gilda Currenti for her professional and personal support; she represented a strong stimulus and inspiration in my research activity.

Last but not least, I deeply thank my family, to be always ready to support and encourage me even in the difficulties, giving me the certainty that I would never have been alone.

Index

Introduction 1
Chapter 1
Numerical Methods: FE Modeling of Ground Deformation, Piezomagnetic and Gravity Fields..... 11
1.1 Governing equations of ground deformation, piezomagnetism and gravity 13
1.2 Numerical model..... 20
1.3 Comparison Between Analytical and Numerical Results ... 23
1.3.1 Piezomagnetic and gravity field generated by pressure source.. ……...24
1.3.2 Piezomagnetic and gravity field generated by intrusive source..... 30
1.4 Discussions 33
Chapter 2
Effects of Heterogeneity and Topography on Piezomagnetic Field..... 35
2.1 Heterogeneity effect 37
2.1.1 Effects of elastic heterogeneity……...37
2.1.2 Effects of magnetic heterogeneity……..41
2.2 Topography effect 47
2.3 Discussions 50
Chapter 3
Application to Real Case Studies at Etna Volcano 53
3.1 Numerical model of Mt Etna..... 56

3.2 Pressure source model: 2005-2006 Etna activity.....58
3.3 Intrusive source model: 2008 Etna Eruption.....69
3.4 Discussions.....85
Chapter 4
FEM and ANN combined approach for predicting pressure sources at Etna volcano.....91
4.1 Forward Problem: FEM solution.....93
4.2 Neural Network model.....100
4.3 Identification results.....103
4.3.1 ANN based inverse model……103
4.3.2 ANN based forward model……111
4.4 Discussions.....114
Conclusions.....116
Bibliography.....119

List of tables

1.1	Pressure source geometry and medium properties.	25
1.2	Intrusive source geometry and medium properties.	31
2.1	Model properties. The magnetic structures J_A and J_B are described in Fig. 2.3.	37
3.1	Source geometry and medium properties by Bonforte et al. (2008).	62
3.2	Gravity variations related to 2005-2006 period observed at the monitoring stations at Mt. Etna after having been corrected for free air effect.	68
3.3	Chi-square values of deformation and magnetic changes for the analytical and the numerical models.	80
4.1	Ranges of the random generated parameters of the source.	97
4.2	Performance indexes *RMSE* and $E\%_{abs}$ for the inversion of analytical and numerical deformation model and for the integrated numerical model.	105
4.3	Performance indexes RMSE and normalized misfits δ_m for two stations located near (A in Fig. 4.4) and far (B in Fig. 4.4) from the summit of volcano.	113

List of Figures

1.1	Computational domain and boundary conditions for the deformation.	21
1.2	Computational domain for magnetic and gravity problem.	22
1.3	Meshed domain of the numerical model. The mesh is refined around the volcano structures and becomes coarser at greater distance..	23
1.4	Comparison between the analytical solutions (color scale) and the numerical results (line). Contour lines are at 0.5 nT intervals. Profiles along NS and EW directions are reported for the analytical (line) and numerical (circles) models.	28
1.5	Comparison between the analytical solutions (color scale) and the numerical results (line) of gravity field.	29
1.6	Displacement at the source wall along a section at z=-800 m in a 3D view. Red and blue colors represent the positive and negative displacement along the x-axis respectively.	32
1.7	Comparison between the analytical solutions (color scale) and the numerical results (line) of piezomagnetic variation generated by a dyke source. Contour lines are at 10 nT intervals.	32
1.8	Comparison between the analytical solutions (color scale) and the numerical results (line) of gravity variation generated by a dyke source. Contour lines are at 5uGal intervals.	33

2.1	Young modulus distribution (a) and Poisson ratio distribution (b).	38
2.2	Total intensity of piezomagnetic field produced by a pressure change (a) and a volume change (b) in a spherical source for the half-space model B, which is homogeneous in magnetic properties and heterogeneous in elastic parameters. Contour lines are at 0.5 nT intervals. The star represents the pressure source location.	39
2.3	Layered structures of the initial magnetization free from stresses. On the left the JA two-layered magnetization structure, on the right the JB three-layered magnetization structure.	42
2.4	Geological based model of Mt Etna by Tibaldi and Groppelli.	44
2.5	The total piezomagnetic field for the half-space models C (a) and D (b). Contour lines are at 0.5 nT intervals.	45
2.6	Total intensity of piezomagnetic field (contour lines at 0.5 nT intervals) for the half-space models E (a) and F (b).	46
2.7	Mesh of the topography of Mt Etna.	47
2.8	The magnetic field changes for a homogeneous magneto-elastic medium with the real topography of Mt Etna. Contour lines are at 0.5 nT.	48
2.9	Total intensity of piezomagnetic field for the models E (a) and F (b) with the real topography of Mt Etna. Contour lines are at 0.5 nT intervals.	49
3.1	Continuous GPS monitoring network at Mt Etna.	54
3.2	Gravity and magnetic monitoring networks at Mt Etna	54
3.3	Distribution of Young Modulus (a) and rock magnetization (b) in numerical model of Mt Etna.	57

3.4	Magnetic measurements at Mt Etna during the period 2005-2006.	59
3.5	Gravity anomaly observed at Mt Etna during the period 2005-2006. Contour lines are at 10 μGal.	60
3.6	Source modeled by Bonforte et al. (2008) represented by an ellipsoidal pressure source and a sliding plane, together with the comparison between the observed and the modelled ground deformation vectors.	61
3.7	Section of the mesh of the computational domain.	63
3.8	Comparison between deformation field observed at the GPS stations at Mt. Etna (blue arrows) and computed deformation field generated by the pressure source (green arrows). Contour lines (at 1 cm intervals) represent the vertical displacement anomaly computed with the numerical model.	64
3.9	Piezomagnetic anomaly (contour lines at 0.1nT) generated by the pressure source. The black circles are the magnetic stations of monitoring network at Mt. Etna.	65
3.10	Thermomagnetic anomaly (contour lines at 1nT) generated by the pressure source. The black circles are the magnetic stations of monitoring network at Mt. Etna. Inset shows the magnetic variations observed at the monitoring stations.	66
3.11	Gravity anomaly (contour lines at 2.5μGal) generated by the pressure source. The black circles are the gravity stations of monitoring network at Mt. Etna.	67
3.12	Schematic map of the Etna summit area covered by the lava flows of the 2008 eruption. Locations of magnetic, gravity and GPS stations are also shown. Inset shows the position of the CSR magnetic reference station.	70

3.13	Magnetic observation at the magnetic stations during the 2008 eruption at Mt Etna.	71
3.14	(A) Radial (rad) and tangengential (tan) tilt components recorded during the 713 May 2008 intrusion. (B) Selected North–South (N–S) and East–West (E–W) position components recorded by the GPS network. The signals are smoothed using a mobile average with a 10-min duration window. The grey box indicates the first phase of the intrusion (Aloisi et al, 2009).	72
3.15	View of the mesh of computational domain, with a high resolution in the areas near the source.	74
3.16	Comparison between analytical solutions (a) and numerical results of model A (b) for the 2008 intrusive source from Napoli et al. [2008]. Piezomagnetic change (contour lines at 2 nT) generated by the intrusive dike (black line). Observed (blue arrows) and computed (red arrows) deformation at the permanent GPS stations are also reported. The recorded magnetic changes are reported in the inset.	75
3.17	Comparison between measured and computed magnetic changes for the analytical and numerical models..	76
3.18	Gravity contributions generated by the intrusive source using the analytical solution. Contour intervals are 1 μGal for δg_1 (a), 10 μGal for δg_2 (b), 2 μGal for δg_3 (c) and 10 μGal for the total gravity change (d). Black circles represent the gravity stations of the monitoring network at Mt. Etna.	77

3.19	Gravity contributions generated by the intrusive source using the numerical model A. Contour intervals are 1 μGal for δg_1 (a), 10 μGal for δg_2 (b), 2 μGal for δg_3 (c) and 10 μGal for the total gravity change (d). Black circles represent the stations of the gravity monitoring network at Mt. Etna.	78
3.20	Piezomagnetic changes, ground deformation (a), and gravity changes (b) caused by the magmatic intrusion in model B. Observed (blue arrows) and computed (red arrows) deformation at the permanent GPS stations are also reported. Contour intervals are 2 nT for the piezomagnetic changes (a) and 10 μGal for gravity changes (b).	81
3.21	Normal displacement to the dike wall in the numerical model D. The dilation profile (opening exaggerated by a factor 300) for an overpressure of 13 MPa is also reported (black line).	84
4.1	Mesh of the computational domain. The mesh has a spatial resolution of 300 m in the summit area and around the source location and becomes coarser at greater distance.	97
4.2	Parallelization of procedure on a cluster of 20 nodes.	99
4.3	Deformation pattern of the vertical component.	99
4.4	Permanent GPS (red circles), gravity (yellow squares) and magnetic (blue triangles) stations of the monitoring networks on Mt Etna. The black rectangle corresponds to the projection on surface of the volume where the sources are located.	100
4.5	Block diagrams of inverse (a) and forward (b) model identification.	102
4.6	Structure of Artificial Neural Network for inversion of geophysical models.	104

4.7	Predicted values of source parameters with respect to output patterns of the testing set for the integrated numerical inversion.	108
4.8	Mean percent error $E\%_{abs}$ for each source parameter using noisy deformation patterns at the inputs of the ANN inverse model.	110
4.9	Mean percent error $E\%_{abs}$ for each source parameter using noisy patterns at the inputs of the integrated ANN inverse model.	110

Introduction

Eruptions are the culmination of long-term evolution in the volcano plumbing system. The complexity of volcanic systems originates from the large variety of physical processes which may precede and accompany the ascent of magma to the Earth's surface and its eruption. During ascent magma interacts with surrounding rocks and fluids and almost inevitably geophysical signal variations are produced.

Monitoring involves geophysical, seismological or geochemical techniques that detect magma movements and associated sub-surface interactions, through physical measurements, which are made both at the earth's surface and within the earth's subsurface.

Over the last decades, new modern techniques of volcano monitoring have been implemented on active volcanoes in order to improve the knowledge of eruptive processes. The characterization of geophysical signals can be a useful tool both for improving the monitoring of

active volcanoes as well as developing a greater understanding of the pre-eruptive mechanisms which produce them.

However, field data alone are not enough for making any quantitative interpretation, but in addition model responses are needed. By examining together field data and model data, the quantitative statement of the structure and dynamics of the volcanoes can be examined. Mathematical models have become key tools, not only to forecast the dynamic of the volcanic activity, but also to interpret a wide variety of geophysical observations, which have provided further insights into the complex dynamics of eruptive processes.

Magma migration inside a volcano edifice generates a wide variety of geophysical signals, which can be observed before and during eruptive processes. In particular, ground deformation, gravity and magnetic changes in volcanic areas are generally recognized as reliable indicators of unrest, resulting from the intrusion of fresh magma within the shallow rock layers. If the volcanic edifice can be assumed to be elastic, contributions to geophysical signal variations depend on surface and subsurface mass redistribution driven by dilation/contraction of the volcanic source. Indeed ground deformation studies provide insight about volume changes in the magma reservoir and the dynamics of dike intrusion processes (Voight et al.1998; Battaglia et al., 2003 Murase et al. 2006). However, deformation data alone are not able to properly constrain the mass of the intrusions. Geodetic studies need to be supported also by gravity observations in order to infer the density of the intrusive body and better define the volcanic source (Carbone et al. 2006). Gravity and deformation

changes are strictly related each other. Indeed, changes in the gravity field cannot be interpreted only in terms of gain of mass disregarding the ground deformation of the rocks surrounding the source. Contributions to gravity changes depend also on surface and subsurface mass redistribution driven by dilation of the volcanic source. Moreover, in volcanic areas, significant correlations were observed between volcanic activity and changes in the local magnetic field, up to ten nanoteslas (Del Negro and Currenti, 2003). These observations were compared with those calculated from volcanomagnetic models, in which the magnetic changes are generated by stress redistribution due to magmatic intrusions at different depth and by the thermal demagnetization at a rather shallow depth. The magnetic data not only allowed the timing of the intrusive event to be described in greater detail but also, together with other volcanological and geophysical evidences, permitted some constraints to be set on the characteristics of propagation of shallow dikes (Del Negro et al., 2004).

The comparison between these observations and geophysical models allowed inferences about volcanic source parameters and detailed descriptions of magma migration, but limited efforts have been made for effective integration of these different data. These geophysical signals are generally interpreted separately from each other and the consistency of interpretations from these different methods is qualitatively checked only a posteriori. Anyway, when the cause of these geophysical signal variations can be ascribed to the same volcanic source, an integrated approach based on different

geophysical data should prove a more efficient and accurate procedure for inferring magmatic intrusions and minimizing interpretation ambiguities (Nunnari et al, 2001; Currenti et al., 2011).

Ground deformation, gravity and magnetic variations due to volcanic sources have been modeled separately using analytical solutions, based on simple homogeneous elastic half-space models (Bonaccorso and Davis, 2004; Carbone et al 2007; Del Negro and Currenti, 2003; Del Negro et al 2004; Napoli et al, 2011). Analytical elastic models are attractive because of their straightforward formulation. The drawbacks of the analytical formulations for modeling volcanic activities are the assumption of simple geometries for the sources embedded in homogeneous elastic half-space. Nevertheless natural characteristics of volcanic areas such as topography or lateral variations of rheological properties may have great influence on the observed signals: such complexities can be treated using numerical methods. The most adequate method to calculate stress and strain and hence deriving associated geophysical signals changes in a given material is the finite element method (FEM). This method allows to overcome these intrinsic limitations and provide more realistic models, which allow considering topographic effects as well as heterogeneous distribution of medium properties.

We dealt with the problem of the interpretation of geophysical data in order to analyze quantitatively the structure and dynamics of volcanoes. Improving forward models with FEM is the starting point for the geophysical processes representation, but the inverse modeling, that deals with the estimate of the parameters of a source that causes

significant changes in geophysical observations recorded by monitoring networks, is the principal goal of modeling in geophysics.

Inverse problems are usually formulated and solved as optimization problems based on iterative procedures, minimizing an objective function that quantifies the misfit between the observed data and the estimated solutions from forward models. Analytical solutions are often used to represent the forward model because of computational convenience and fast computer implementation (Currenti et al., 2005; Nunnari et al., 2005). Numerical solutions allow to overcome the intrinsic limitations of analytical models, but the use of numerical forward models in iterative methods is computationally expensive since the estimate of the objective function requires to perform a full FEM analysis at every iteration step. As traditional optimization algorithms cannot "learn", they cannot benefit from solutions obtained previously for similar problems and each new inversion requires the minimization procedure to be re-iterated.

Recently, Artificial Neural Networks (ANNs) have been introduced to solve the inverse problem in many research applications (Haykin, 1999, Arena et al., 1998). The main advantage of inverting with ANNs consists in the availability of an approximation of the inverse model, avoiding a search for the minimum and speeding up the computation of the optimal solution that fits the observed data. ANNs have been widely used to invert geophysical models based on straightforward analytical solutions (Langer et al., 1996; Maugeri et al., 1996; 1997; Nunnari et al. 2001) because of low computational effort. On the contrary, FEM-based numerical solutions are not often

combined to ANN inversion scheme because they are time-consuming both in length of time required to design a mesh and in actual computation time. With the advent of today's powerful computer resources and the automation of mesh generation and FEM analysis, hybrid schemes based on FEM and ANN have been proposed in different applications (Hacib et al., 2007; Preda et al, 2002; Ziemianski, 2003; Ajmera et al., 2008; Szidarovszky et al., 1997; Chamekh et al, 2009; Muliana et al., 2002; Saltan et al., 2007; Umbrello et al., 2008).A promising method to address the issue of geophysical modeling should be a hybrid approach using FEM and ANN to model jointly geophysical signals as deformation, gravity and magnetic signals (Di Stefano et al, 2010). We investigate the ability of a hybrid procedure in which ANNs are used for system identification of forward and inverse geophysical models solved by FEM.

The discussed approaches for interpretation of geophysical data are successfully applied to Etna volcano, which offer exemplary case studies to validate the capability of the proposed integrated approach for imaging the pressurization and intrusive processes occurring in the volcano. Volcanological tradition is consolidated at Mt Etna and advanced monitoring networks enabled collecting multi-disciplinary data during the frequent eruptions in recent years (Rymer et al, 1998). Geodetic, gravity and magnetic investigations have played an increasingly important role in studying the eruptive processes at Mt Etna (Napoli et al., 2008; Bonforte et al., 2008; Carbone et al., 2007; Del Negro et al., 2004; Bonaccorso et al, 2011). Moreover, as indicated by geological evidences and seismic tomography (Chiarabba

et al., 2000; Tibaldi and Groppelli, 2002), the Etna volcano is elastically inhomogeneous and rigidity layering and heterogeneities are likely to affect the magnitude and pattern of observed signals (Currenti et al., 2007; 2009). So the volcano complex structure can be well represented by the proposed numerical models.

The aim of this thesis is, starting from the simplified analytical geophysical models to reach the more realistic integrated numerical model for ground deformation, magnetic and gravity field variations generated from a volcanic source. Indeed the FEM should provide a more precise description including realistic features for the source shape, the topographic relief, the elastic medium heterogeneities and the density stratifications.

In *Chapter 1* a joint forward formulation of deformation, piezomagnetic and gravity data is provided through a FEM coupled model, in order to overcome the limitation proper of the analytical forward in terms of half-space and at the same time don't mistreat the multi-parametric approach. All the geophysical changes were evaluated by solving an elastic homogeneous problem both for pressure source and intrusive sources, in order to compare analytical and numerical solution. 3-D elastic models based on finite element method (FEM) have been developed to compute piezomagnetic and gravity fields caused by magmatic overpressure and dyke sources. We solved separately (i) the elastostatic equation for the stress field and (ii) the coupled Poisson's equation for magnetic and gravity potential field.

Once tested the accuracy of FEM solution, the effects of medium heterogeneities and topography were evaluated in *Chapter 2*. The numerical computations were focused on a more realistic modelling of Etna volcano, where remarkable geophysical changes have been observed during eruptive events. The effects of topography and medium heterogeneities were evaluated considering different multilayered crustal structures constrained by seismic tomography and geological evidences.

The FEM approach presented here allows considering a picture of a fully 3-D model of Etna volcano, which could advance the reliability of model-based assessments of magnetic observations.

In *Chapter 3* successively a 3D finite element modeling was set up to analyze two case studies: the first was the 2005-2006 inflation period at Mt Etna, the second one was the magmatic intrusion occurring in the northern flank of Etna during the onset of the 2008 eruption.

A 3D numerical model based on Finite Element Method (FEM) is implemented to jointly evaluate geophysical changes caused by dislocation and overpressure sources in volcanic areas. A coupled numerical problem was solved to estimate ground deformation, gravity and magnetic changes produced by stress redistribution accompanying magma migration within the volcano edifice.

A multi-layered crustal structure of the volcano constrained by geological models and geophysical data was considered. Geodetic and gravity data provide information on the strain field, while piezomagnetic changes give constraints on the stress field. Therefore, the integrated modeling gives insights on Mt Etna rheology and dike

overpressure involved in the magma propagation and improves understanding of dike emplacement in the northern sector of the volcano.

The last challenging scope of this thesis, described in *Chapter 4*, was to solve a numerical integrated inverse problem. A hybrid approach for forward and inverse geophysical modeling, based on Artificial Neural Networks (ANN) and Finite Element Method (FEM), is proposed in order to properly identify the parameters of volcanic pressure sources from geophysical observations at ground surface. The neural network is trained and tested with a set of patterns obtained by the solutions of numerical models based on FEM. The geophysical changes caused by magmatic pressure sources were computed developing a 3-D FEM model with the aim to include the effects of topography and medium heterogeneities at Etna volcano. ANNs are used to interpolate the complex non linear relation between geophysical observations and source parameters both for forward and inverse modeling. The results show that the combination of neural networks and FEM is a powerful tool for a straightforward and accurate estimation of source parameters in volcanic regions.

Chapter 1

Numerical Methods: FE Modeling of Ground Deformation, Piezomagnetic and Gravity Fields

Before eruption, magma chamber pressurization and magma ascent to the Earth's surface force surrounding crustal rocks apart and this perturbs stress distributions, commonly producing variations in the magnetization and density of rocks, resulting in a local magnetic field and gravity field change (Nagata 1970; Pozzi 1977). Gravity and

piezomagnetic changes are calculated by combining the Cauchy–Navier equation for elastic equilibrium and the Poisson's equation for the magnetic and gravity potential (Sasai 1986; Utsugi et al. 2000).

The analytical solutions are derived by employing important simplifications and approximations (Sasai, 1991a; 1991b; Utsugi et al., 2000). Most of the analytical formulations are based on the assumption of a volcanic source embedded in a homogeneous magneto-elastic half-space medium (Sasai, 1991b). Analytical elastic models are attractive because of their straightforward formulation.

However, volcanic areas are usually characterized by severe heterogeneities and irregular topography that are responsible for significant effects. Although numerical procedures have been applied in ground deformation studies to estimate how topography and heterogeneity can affect the deformation field solution (Williams and Wadge 1998; Williams and Wadge 2000; Cayol and Cornet 1998; Lungarini et al. 2005; Trasatti et al, 2008; Bonaccorso et al., 2005; Currenti et al., 2008), few studies have been performed on the piezomagnetic and gravity field. We developed a coupled numerical model using the Finite Element Method to compute jointly the deformation, gravity and magnetic changes caused by dislocation and pressure sources. The FEM is suitable to easily solve the model equations and to account for topography and medium heterogeneity, which can alter the estimate of the investigated geophysical changes.

Comparisons are made between analytical and numerical solutions both for piezomagnetic and gravity anomalies produced by pressure

sources and dislocation sources embedded in a homogeneous half-space elastic medium, with the aim to properly set up the model and verify the accuracy of the numerical solution.

1.1 Governing equations of ground deformation, piezomagnetism and gravity

In order to find the state of stress and displacement that results from the application of certain loads or boundary displacement, it is necessary to solve a set of three coupled partial differential equations known as "equations of stress equilibrium". These equations are found by using the Newton's second law and can be expressed in the following vector/matrix form:

$$\nabla \cdot \boldsymbol{\sigma} + \rho \mathbf{F} = \rho \frac{\partial^2 \mathbf{u}}{\partial t^2} \qquad (1.1)$$

Where **F** is the body force, $\boldsymbol{\sigma}$ is the stress tensor and ρ is the density of the material.

The equations of motion, along with the strain-displacement relations and the stress-strain relations, constitute a set of equations in which the number of unknowns is equal to the number of equations. In the frequently occurring case in which the rock is in static equilibrium, or in which the displacements are occurring very slowly, the right-hand sides of Equation (1.1) can be neglected.

Governing equations of continuous medium need to be complemented with additional constitutive equations and state laws in order to fully

describe the physics of any particular continuous medium. We analyzed the physics of elastic medium, in which the stress is linearly proportional to the strain and the latter is fully recoverable. If we assume that rocks is a linear elastic material equations of stress equilibrium (2.1) can be expressed in terms of the displacements. We first combine the elastic strain-displacement relations

$$\varepsilon = \frac{1}{2}\left[\nabla \cdot \mathbf{u} + (\nabla \cdot \mathbf{u})^T\right] \tag{1.2}$$

and the elastic stress-strain relations, namely Hooke's law

$$\sigma_{ij} = 3K\left(\frac{1}{3}\varepsilon_{kk}\delta_{ij}\right) + 2G\left(\varepsilon_{ij} - \frac{1}{3}\varepsilon_{kk}\delta_{ij}\right) \tag{1.3}$$

where K is the bulk modulus and G is the shear modulus.

Then, substituting the result into the equations of motion and expressing it in a matrix form, we obtain the Navier equations.

$$(\lambda + G)\nabla(\nabla \cdot u) + G\nabla^2 u + \rho F = 0 \tag{1.4}$$

Subsurface stress and displacement fields caused by dislocation and pressure sources necessarily alter the density distribution and the magnetization of the surrounding rocks that in turn affects the gravity and the magnetic fields, respectively.

In order to evaluate the piezomagnetic field, the computation of the stress field at depth is required (Sasai, 1991b). Since piezomagnetic changes are strictly related to stress fields of the elastic medium, the stress field and the piezomagnetic changes produced by volcanic pressure sources need to be modeled jointly.

The change ***ΔJ*** in rock magnetization ***J*** at an arbitrary point, associated with mechanical stress σ, can be expressed as follows:

$$\Delta\mathbf{J} = \frac{3}{2}\beta\mathbf{T}\cdot\mathbf{J}$$
$$\mathbf{T}_{kl} = \sigma_{kl} - \frac{1}{3}\delta_{kl}\Theta \qquad (1.5)$$
$$\Theta = \sigma_{xx} + \sigma_{yy} + \sigma_{zz}$$

where β is the stress sensitivity, σ_{kl} are the components of the stress tensor, δ_{kl} is the Kronecker delta. The piezomagnetic change depends on the deviatoric stress tensor ***T***, that is obtained from the stress tensor ***σ*** subtracting the isotropic stress $\frac{1}{3}\delta_{kl}\Theta$. Using Hooke's law, components of stress tensor can be expressed as a function of displacement vector:

$$\sigma_{kl} = \lambda\delta_{kl}\mathrm{div}\mathbf{u} + \mu\left(\frac{\partial u_k}{\partial x_l} + \frac{\partial u_l}{\partial x_k}\right) \qquad (1.6)$$

where λ and μ are the Lamé's constants. Substituting Eq. (1.6) in Eq. (1.5) we obtain the stress induced magnetization expressed by displacement components (ΔJ_{kl} is the *l*-th component of the incremental magnetization produced by the *k*-th component of the initial magnetization):

$$\Delta J_{kl} = J_k\beta\mu\left[\frac{3}{2}\left(\frac{\partial u_k}{\partial x_l} + \frac{\partial u_l}{\partial x_k}\right) - \delta_{kl}\mathrm{div}\mathbf{u}\right] \qquad (1.7)$$

In magnetostatic problem, where no currents are present, the problem can be solved using a scalar magnetic potential. In a current-free region, a scalar magnetic potential W_k can be related to magnetic field ***H***, according to the equation:

$$\mathbf{H} = -gradW_k \tag{1.8}$$

The magnetic induction ***B*** can be expressed as follows in the SI system:

$$\mathbf{B} = \tilde{\mu}\mathbf{H} + \tilde{\mu}\mathbf{\Delta J_k} \tag{1.9}$$

where $\tilde{\mu}$ is the magnetic permeability (in this instance replacing the classical notation μ to avoid confusion with the rigidity modulus). Since Gauss' law holds div***B***=0 and the source of the magnetic field is the magnetization alone, the piezomagnetic potential satisfies the following equation:

$$\nabla^2 W_k = -div\mathbf{H} = div\mathbf{\Delta J_k} \tag{1.10}$$

The gravity change δg, related to the density redistribution, can be calculated by solving the following Poisson's differential equation for the gravitational potential ϕ_g (Cai & Wang 2005):

$$\nabla^2 \phi_g = -4\pi G \Delta\rho(x, y, z) \tag{1.11}$$

where G denotes the universal gravitational constant and $\Delta\rho$(x, y, z) is the change in the density distribution. Generally, the total gravity change at a benchmark on the ground surface is given by:

$$\delta g(x, y, z) = -\frac{\partial \phi_g}{\partial z} + \delta g_0 \tag{1.12}$$

where δg_0 represents the "free air" gravity change accompanying the uplift of the observation site. The "free air" gravity change, in first approximation, is given by:

$$\delta g_0 = -\gamma \delta h \qquad (1.13)$$

where γ is the free-air gravity gradient (generally γ =308.6 μGal/m) and δh the elevation change. The density variations related to the subsurface mass redistribution can be accounted for by three main terms:

$$\Delta\rho(x,y,z) = \delta\rho_1 - \mathbf{u}\cdot\nabla\rho_0 - \rho_0\nabla\cdot\mathbf{u} \qquad (1.14)$$

where $\boldsymbol{u}$ is the displacement field, ρ_0 is the embedding medium density and $\delta\rho_1$ is the density change due to the input of intrusive mass from remote distance. The first term originates from the density change related to the introduction of the new mass into the displaced volume. The second term is due to the displacement of density boundaries in heterogeneous media, and the third term is the contribution due to the volume change arising from compressibility of the surrounding medium (Bonafede & Mazzanti, 1998). Each term in the density variation contributes to the total gravity change observed at the ground surface. Therefore, the gravity changes are made up by four different contributions:

$$\delta g = \delta g_0 + \delta g_1 + \delta g_2 + \delta g_3 \qquad (1.15)$$

where δg_1, δg_2 and δg_3 arise from the three terms in Eq. 1.14.

Usually, δg_1 is only accounted for the excess mass above the reference level corresponding to the upheaved portion of the free surface. A simple Bouguer correction is applied assuming the mass distributed as an infinite slab with thickness equal to the uplift.

In mountainous regions, a more complex terrain correction must be performed. Terrain effect and Bouguer anomalies can cause γ to differ by up to 40% from its theoretical value (Rymer, 1994). Furthermore, in volcanic areas density heterogeneity of the subsurface structures can contribute to density variation through the displacement of the buried density interfaces. The δg_1 and δg_3 terms highlight that the computation of the displacement field at depth is required in order to evaluate these gravity contributions. It calls that changes in the gravity field cannot be interpreted only in term of additional mass input disregarding the deformations of the surrounding rocks (Bonafede and Mazzanti 1998; Currenti et al., 2007; Charco et al., 2004, Charco et al., 2006).

Since gravity and piezomagnetic changes are strictly related to stress and deformation fields, ground deformation, magnetic and gravity changes produced by volcanic sources need to be jointly modeled (Sasai et al. 1991; Okubo et al. 2004; Hagiwara, 1977).

Over the last decades, straightforward analytical solutions for deformation, magnetic and gravity field have been devised under the assumption of homogeneous elastic half-space medium and for simplified geometric sources (Sasai, 1991a; 1991b; Utsugi et al., 2000). Surface displacements in a homogeneous elastic half-space

have been described by Mogi (1958) for a spherical source, by Yang et al. (1988) for ellipsoidal sources, by Okada (1985; 1992) for a rectangular fault. Analytical solution to model gravity changes which are expected to accompany crustal deformation due to volcanic sources have been devised and widely used in literature (Jousset et al. 2003; Okubo 1992). Most of the analytical formulations for modeling inflation and deflation episodes describe the effects caused by sources with a specific shape such as spheres (Hagiwara, 1977), ellipsoids (Battaglia & Segall, 2004) or rectangular prisms (Okubo & Watanabe, 1989). Also the analytical formulation of the different mechanisms, which can be the cause of volcanomagnetic signals, has advanced considerably (Adler et al., 1999). While thermomagnetic effects are mainly concerned with temperature changes within the volcano edifice (Blakely, 1996), piezomagnetism and electrofiltration process are both related to stress variations (Zlotnicki and Le Mouel, 1988). As for the piezomagnetic field, Sasai (1991) succeeded to devise an analytically expression for the Mogi model, while Utsugi et al., (2000) calculated the solutions for strike-slip, dip-slip, and tensile-opening of a rectangular fault with an arbitrary dip angle. As for electrokinetic effects, the analytical form of magnetic fields by an inclined vertical source in inhomogeneous media was devised by Murakami (1989).

Nevertheless the advantages of analytical models due especially to their simplicity, more elaborated models are required to overcome their intrinsic limitations and provide more realistic models, which consider topographic effects as well as complicated distribution of medium properties.

We developed a coupled numerical model using the Finite Element Method to compute jointly the deformation, gravity and magnetic changes caused by dislocation and pressure sources. Using the commercial software COMSOL Multiphysics (2008) we numerically solve: (i) the elastostatic problem for the elastic deformation field and its derivatives, (ii) the coupled Poisson's problem for gravity field (Currenti et al., 2007), (iii) the coupled Poisson's problem for magnetic potential field (Currenti et al., 2009).

1.2 Numerical model

A computational domain of a 100x100x50 km is considered for the deformation field calculations. As for boundary conditions, u_x and u_y displacements are fixed to zero at the lateral boundaries of the domain and vertical displacement u_z is fixed to zero at the bottom boundary, approximating the vanishing displacement at infinity. The domain size is important because of the assignment of the boundary conditions. Since in numerical methods the size domain is finite, these boundary conditions are implemented by considering a domain big enough that the assumption of zero displacement at the boundary does not affect the solution in the interested area (Fig.1.1). The upper boundary is stress free and represents the ground surface, to which the condition $\boldsymbol{\sigma} \cdot \mathbf{n} = 0$ is imposed, where $\boldsymbol{\sigma}$ is the stress tensor and $\boldsymbol{n}$ is the normal vector to the ground surface.

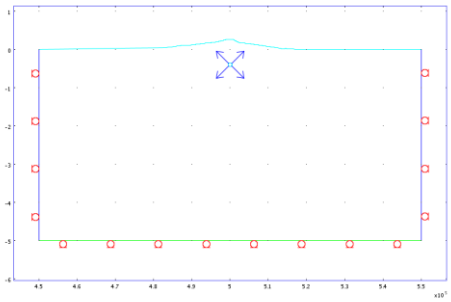

Figure 1.1 Computational domain and boundary conditions for the deformation problem.

In order to solve the Poisson's equation (Eqs. 1.10 and 1.11) the potential or its normal derivative are to be assigned at the boundaries of the domain (Dirichlet or Neumann boundary conditions), which is extended along the z direction of 50 km to finally obtain a 100x100x100 km computational domain (Fig.1.2) . Along the external boundaries zero gravity potential is specified using Dirichlet boundary conditions, while the magnetic field is assumed to be tangential by assigning a Neumann condition on the magnetic potential $\frac{\partial W_k}{\partial n} = 0$.

The magnetic problem is made unique by setting the potential to zero at an arbitrary point on the external boundary. The continuity of the gravity and magnetic potential, of the tangential component of $\boldsymbol{H}$, of the normal component of $\boldsymbol{B}$ on the ground surface and on the source wall are also warranted.

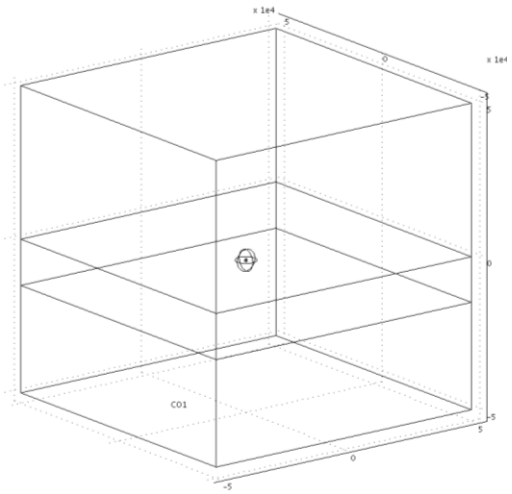

Figure 1.2 Computational domain for magnetic and gravity problem.

As for finite elements size, the meshing operation is a fundamental step: the smaller the elements, the more precise the solution. However, if too small elements are used, the number of nodes in which the equations are to be solved increases and computation becomes heavy (Fig. 1.3).

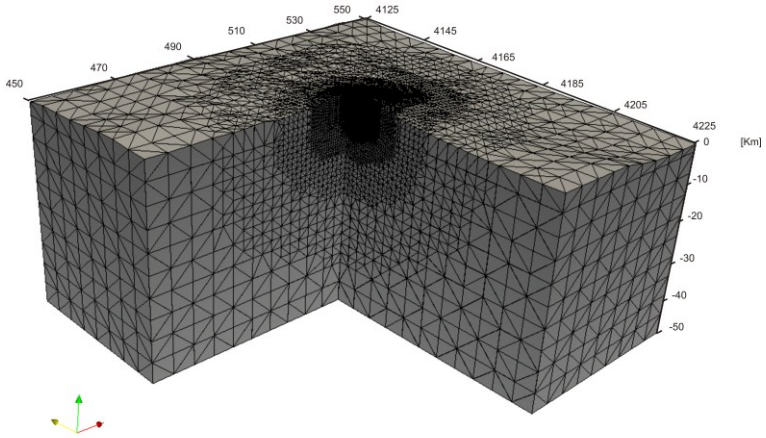

Figure 1.3. Meshed domain of the numerical model. The mesh is refined around the volcano structures and becomes coarser at greater distance.

1.3 Comparison Between Analytical and Numerical Results

The great advantage of the finite element method is its flexibility: by dividing the computational domain in small elements (meshing operation), it is possible to associate to each element different physical properties such as elastic parameters or densities. Since smaller or curvilinear elements can be used in order to fit every kind of roughness, complex shapes of the computational domain or sources can be considered.

The accuracy of the numerical solution depends heavily on the mesh resolution and the computational domain size. To set up the model properly, benchmark tests are carried out to calculate both stress field and the piezomagnetic and gravity changes. To verify the accuracy of the numerical solution, we compared analytical and numerical solutions of piezomagnetic and gravity fields generated by pressure sources and dislocation sources embedded in a homogeneous half space elastic medium.

1.3.1 Piezomagnetic and gravity field generated by pressure source

Magma rises through fractures from beneath the crust because it is less dense than the surrounding rock. When the magma cannot find a path upwards it pools into a magma chamber. As more magma rises up below it, the pressure in the chamber grows. This phenomenon is commonly ascribed to a *pressure source* that describes the effect of dilatation caused by accumulation of magma or gas in a reservoir. As for pressure sources, a variety of mechanisms have been proposed in the past: one of the first and probably the most employed was proposed by Mogi (1958), who studied the response of a homogeneous, isotropic and elastic half-space to a isotropic dilatation point in axi-symmetric geometry. A more general reservoir

description is the 3-D point-source ellipsoidal cavity studied by Davis (1986).

In our numerical model, the piezomagnetic and gravity changes produce by a pressure source are computed for a spherical source located in the upper eastern flank of Etna in an area that has been a preferential pathway of rising magma and a region of intermediate magma storage (Bonforte et al., 2008). The source has an overpressure of 200 MPa and radius 0.5 km, buried at a depth of 3000 m (Table 1.1) in a homogeneous half-space medium whose medium parameters are the following: Young modulus E=50 GPa, Poisson's ratio ν=0.25, initial magnetization J=5 A/m, density of rocks ρ=2500 kg/m^3. The computational domain is meshed into 125,344 isoparametric, and arbitrarily distorted tetrahedral elements connected by 21,774 nodes. The mesh is refined around the magmatic sources and becomes coarser at a greater distance. Lagrange cubic shape functions are used in the computations, since the use of lower order elements worsens the accuracy.

Table 1.1 – Pressure source geometry and medium properties.

Model Parameters	Value
Curie Depth	18000 m bsl
Magnetic Inclination	51°
Magnetic Declination	1°
Stress Sensitivity	$2x10^{-9}$ Pa^{-1}
Pressure change	200 MPa

Depth	-1500 m bsl
Radius	500 m
Xc	500 UTM km
Yc	4178 UTM km

For the computation of the piezomagnetic field change, it is assumed that the direction of the initial magnetization is the same as that of the geomagnetic field (I=51° and D=1°). The remanent magnetization of rocks of Etna, that were emplaced about 0.50 Ma (Branca et al., 2007) after the last field reversal (0.78 Ma; Tauxe et al., 1992), is generally much greater than induced magnetization (Königsberger ratio is > 1; see e.g. Rolph, 1992; Tric et al., 1994). Considering the Curie temperatures, which for Etna's rocks were generally found near T_C ≈550°C (Del Negro and Ferrucci, 1998), and a vertical geothermal gradient of 30 °C/km measured in deep boreholes (AGIP, 1977), we set the depth of the Curie isotherm at 18 km bsl.

The numerical solutions of a homogeneous magneto-elastic half-space are compared with the analytical ones. The analytical solutions of the elastostatic and magnetic problems are obtained using the simple and common Mogi model embedded in a homogeneous Poisson's medium (Mogi, 1958; Sasai, 1991b). We report on the changes in the north component (ΔX), in the east component (ΔY), and in the vertical component (ΔZ) of the magnetic field. We also computed the total magnetic field intensity (ΔF) defined as:

$$\Delta F = \Delta X \cos D \cos I + \Delta Y \sin D \cos I + \Delta Z \sin I \qquad (1.16)$$

since it is the parameter measured by scalar magnetometers that are usually installed in volcano monitoring networks (Del Negro et al., 2002). The piezomagnetic variation is evaluated at a height of 4 m from the ground surface, the height of the magnetic sensors installed on Etna volcano.

A good match between the analytical and numerical solutions (model A) is obtained (Fig. 1.4).

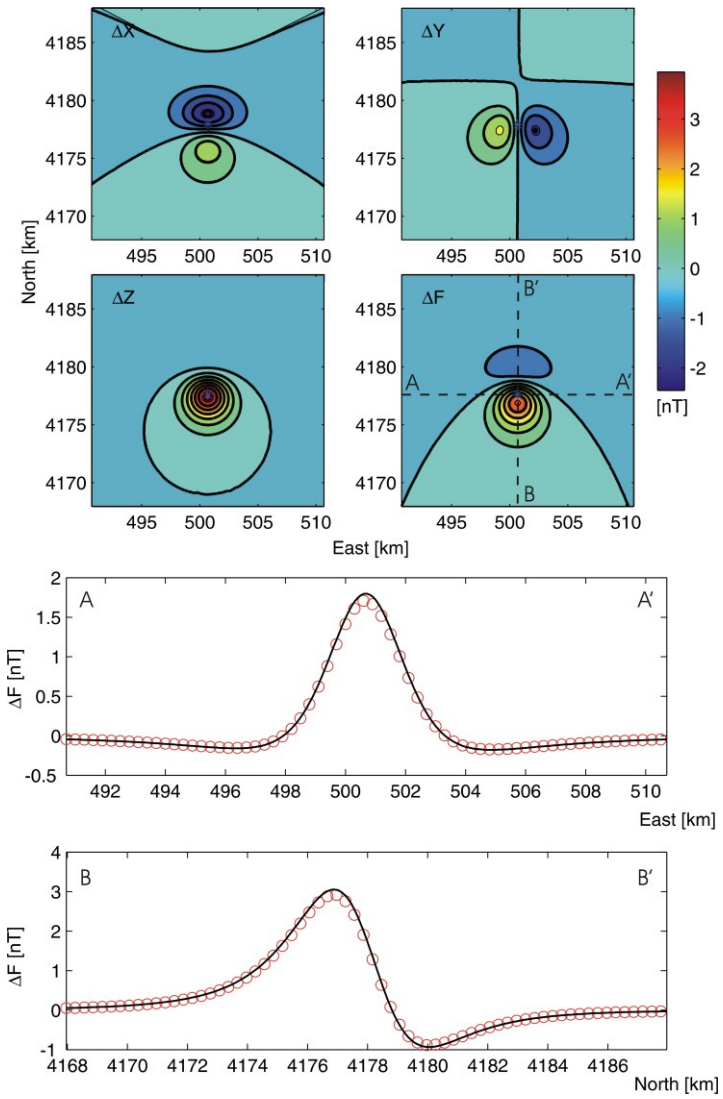

Figure 1.4 – Comparison between the analytical solutions (color scale) and the numerical results (line). Contour lines are at 0.5 nT intervals. Profiles along NS and EW directions are reported for the analytical (line) and numerical (circles) models.

Then the gravity changes caused by the expansion of a spherical source embedded in a homogeneous Poisson's medium ($\lambda=\mu$) are compared with the analytical expressions (Hagiwara 1977). Since the different contributions to density variation (Eq. 1.14) are linearly summed in the Poisson's equation, the three terms δg_1, δg_2 and δg_3 can be solved separately thanks to the superposition principle.

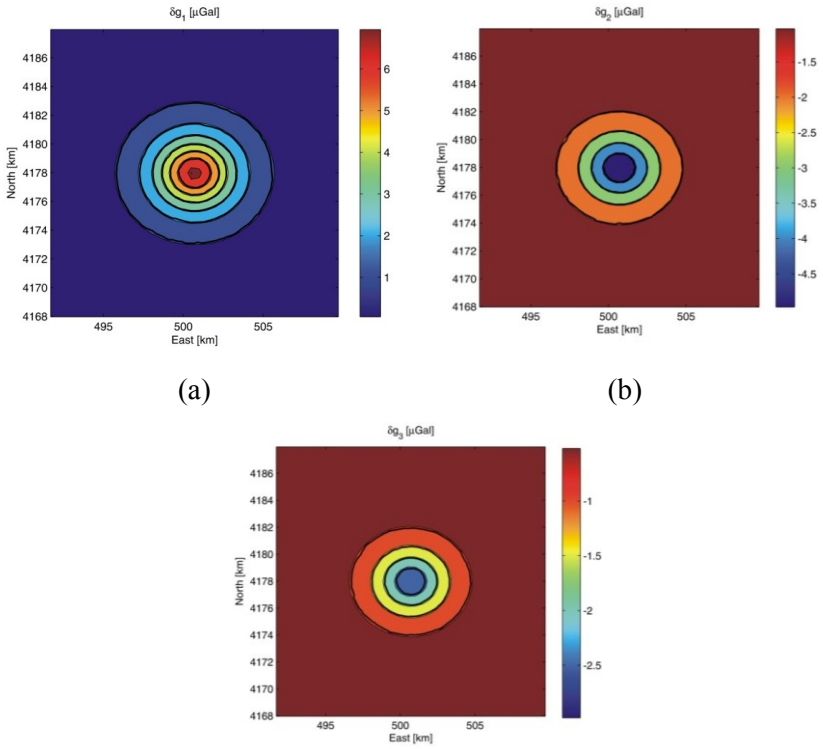

Figure 1.5 Comparison between the analytical solutions (color scale) and the numerical results (line) of gravity field.

We analyzed the case in which the source inflates without addition of new mass: $V'\rho'=V\rho$, where V and V' are the source volume before and after the inflation respectively and ρ and ρ' are the source density before and after the inflation. In such a case the overall gravity change ($\delta g_1+\delta g_2+\delta g_3$) due to the deformation of an homogeneous half-space caused by a point source vanishes identically (Walsh and Rice, 1979). Numerical results well agree with the analytical ones (Fig. 1.5).

1.3.2 Piezomagnetic and gravity field generated by intrusive source

After having investigated pressure sources, we computed the numerical solution of piezomagnetic field and gravity field generated by intrusive source, that are the most common sources at Mt Etna. A classic mechanism of magma uprising is related to intrusive processes characterizing the emplacement of dikes. An intrusive dike is an igneous body with a very high aspect ratio, which means that its thickness is usually much smaller than the other two dimensions.
A dike can be represented by an opening fault (tensile slip). Tensile dislocation theory has been applied with success to the case of a rectangular shaped source with tensile opening in an elastic homogeneous half-space (Okada, 1985; Yang and Davis, 1986).

In the numerical model the intrusion source is simulated as a discontinuity surface by introducing the mesh elements in pairs along the surface rupture. A given displacement in two opposite directions is applied at the two dike faces.

The source is located at the axis origin and it has an opening of 2 m, buried at a depth of 300 m (Table 1.2) in a homogeneous half-space medium whose medium parameters are the following: Young modulus E=50 GPa, Poisson's ratio ν=0.25, initial magnetization J=8 A/m, density of rocks ρ=2500 kg/m^3.

Table 1.2 – Intrusive source geometry and medium properties.

Model Parameters	Value
Curie Depth	18000 m bsl
Magnetic Inclination	51°
Magnetic Declination	1°
Stress Sensitivity	$2x10^{-9}$ Pa^{-1}
Dyke Opening	2 m
Depth	-300 m
Length	1000 m
Width	1000 m

In Fig.1.6 it is showed the horizontal displacement at the dyke wall along a section of the domain at z=-800 m.

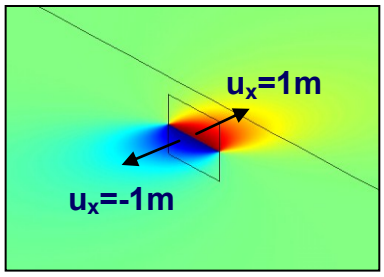

Figure 1.6 Displacement at the source wall along a section at z=-800 m in a 3D view. Red and blue colors represent the positive and negative displacement along the x-axis respectively.

Comparison between analytical (Utsugi et al. [2000] for magnetic field, Okubo [1992] for gravity field) and numerical solutions are performed to validate the numerical solution.

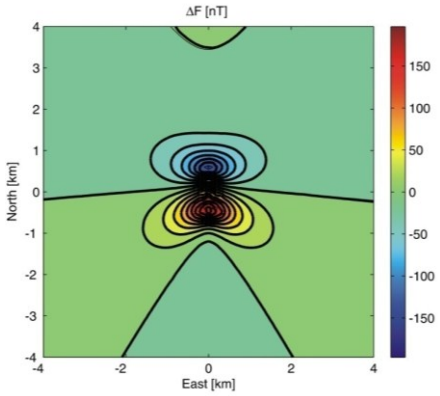

Figure 1.7 Comparison between the analytical solutions (color scale) and the numerical results (line) of piezomagnetic variation generated by a dyke source. Contour lines are at 10 nT intervals.

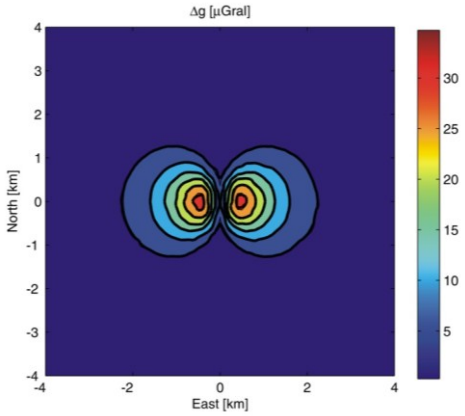

Figure 1.8 Comparison between the analytical solutions (color scale) and the numerical results (line) of gravity variation generated by a dyke source. Contour lines are at 5uGal intervals.

Also for the piezomagnetic and gravity changes generated by an intrusive source there is a good match between analytical and numerical solutions, as showed in Fig. 1.7 and 1.8.

1.4 Discussions

Piezomagnetic and gravity fields produced by pressurized volcanic sources and dyke sources were evaluated by finite element models. The FEM allows us to consider a more realistic picture of volcanic framework by including (i) the topography, (ii) the magnetic heterogeneities of the medium and (iii) the elastic properties distribution. In this section we did not intend to interpret geophysical

changes at Mt Etna as those due to volcanic eruptions, but rather define the numerical model an test the accuracy.

Benchmark tests were carried out comparing the analytical and numerical results of piezomagnetic and gravity field both for pressure sources and intrusive sources.

Our findings highlight that the differential equations of ground deformation, magnetic and gravity field are solved with good accuracy with FEM model. The numerical model is able to represent the geophysical changes, with the possibility to include the complexity of the volcano structure, overcoming the limitations of analytical models.

Chapter 2

Effects of Heterogeneity and Topography on Piezomagnetic Field

The first attempts to estimate the effect of heterogeneity in rock magnetization were carried out solving a 2D numerical model for dislocation source (Zlotnicki and Cornet, 1986) and pressure source (Oshiman, 1990). Recently, Okubo and Oshiman (2004) derived a semi-analytical solution to assess the effects of layered elastic medium on piezomagnetic changes. These previous studies found that neglecting non-uniform distribution of either rock magnetization or elastic properties can introduce underestimations in the interpretation of piezomagnetic fields. Besides the medium heterogeneity, also the topography can alter the estimate of the piezomagnetic field. Using a

numerical method based on BEM, Sakanaka (1997) showed that irregular piezomagnetic changes can arise in a 2D homogeneous medium because of local stress concentration on jagged topography. Using the Finite Element Method (FEM) Yamazaki & Sakai (2006) also observed that local piezomagnetic changes occur in presence of strong slope changes.

Although these previous studies have shown the role played by heterogeneity and topography on piezomagnetic fields, to date most of the models generally used in volcanic areas are based on analytical solutions. With the aim of considering a more realistic description of Mt Etna, we developed the FEM-based numerical model to solve the piezomagnetic field, including not only complicated distributions of both rock magnetization and elastic rigidity, but also the real topography of the studied area. In Currenti et al. (2007) several tests were carried out to appraise the influence of topography and medium heterogeneities on gravity field. In this chapter elastic finite element models are applied to investigate the effects of topography and medium heterogeneities on the piezomagnetic field produced by volcanic pressure sources.

We used the same computational framework described in the previous section for investigating the heterogeneity and topography effect. The source parameters are reported in Table 1.1. Initially, we studied the perturbations caused by the medium heterogeneity using different model parameters. Successively, we took the real topography of Mt Etna into account.

2.1 Heterogeneity effect

We investigated the effects of medium heterogeneity using different model parameters (Table 2.1). All the results can be compared to the model A in Table 2.1, that corresponds to the medium parameters of the homogeneous model whose results are reported in section 1.3.1.

Table 2.1 – Model properties. The magnetic structures J_A and J_B are described in Fig. 2.3.

Model	Elastic Parameter	Magnetization
A	E=50 GPa, ν=0.25	J=5 A/m
B	Heterogeneous	J=5 A/m
C	E=50 GPa, ν=0.25	J_A
D	E=50 GPa, ν=0.25	J_B
E	Heterogeneous	J_A
F	Heterogeneous	J_B

2.1.1 Effects of elastic heterogeneity

Firstly, we evaluated the effect of elastic heterogeneity on the piezomagnetic field while the magnetic properties are assumed homogeneous (model B). A medium for the subsurface structure of Mt Etna is considered by assigning the elastic material properties derived from seismic tomography data to the domain (Patané et al., 2006). We used P-wave and S-wave seismic velocities to define the Young

modulus using the following equation (Kearey and Brooks, 1991):

$$E = V_p^2 \rho \frac{(1-2\nu)(1+\nu)}{1-\nu} \tag{2.1}$$

where V_p is the seismic P-wave propagation velocity, and ρ is the density of the medium, which was set at an average value of 2500 kg/m^3 (Corsaro and Pompilio, 2004). Instead, the values of Poisson's ratio were obtained using the equation (Kearey and Brooks, 1991):

$$\nu = [(V_p / V_s)^2 - 2]/[2(V_p / V_s)^2 - 2] \tag{2.2}$$

where V_s is the seismic S-wave propagation velocity. On the basis of Eqs. (2.1) and (2.2), within the computational domain the Young modulus varies from 11.5 GPa to 133 GPa, while the Poisson ratio is in the range 0.12-0.32.

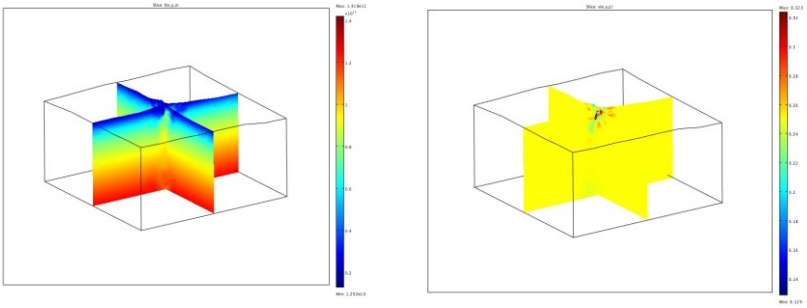

(a) (b)

Figure 2.1. Young modulus distribution (a) and Poisson ratio distribution (b).

To compare the analytical solution with the numerical ones, a

reference surface at 1500 m asl, which represents the average altitude of Etna's topography, is considered. Therefore, in the numerical models the source is positioned at 1500 m bsl with a relative distance from the reference surface of 3000 m, as in the analytical model. The amplitude of the piezomagnetic field does not change significantly with respect to the homogeneous model. Only a slight change in the shape is observed due to smooth variations in the elastic parameters (Fig. 2.2a).

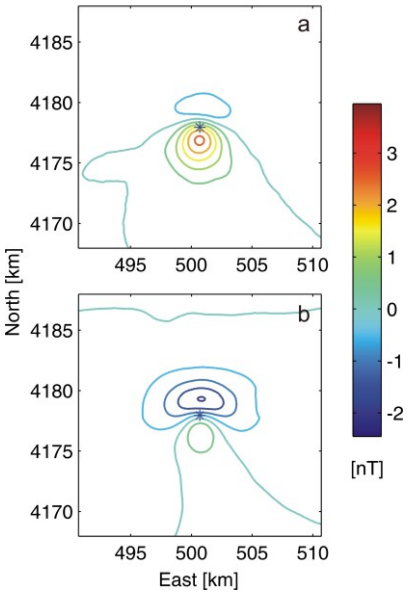

Figure 2.2 –Total intensity of piezomagnetic field produced by a pressure change (a) and a volume change (b) in a spherical source for the half-space model B, which is homogeneous in magnetic properties and heterogeneous in elastic parameters. Contour lines are at 0.5 nT intervals. The star represents the pressure source location.

The small sensitivity of piezomagnetic variations to the elastic structure can be attributed to the assumption of a pressure change at the source wall instead of a volume change as in Okubo and Oshiman (2004). The stress and the piezomagnetic fields produced by a center of dilatation (COD) coincide with those generated by a center of pressure (COP) in a homogeneous elastic half-space (A model) where the pressure change can be related to the volume change through the Lamé constants (Currenti et al., 2008c). The piezomagnetic solution is proportional to the moment of strain nucleus C that can be expressed in terms of ΔV or ΔP as:

$$C = \frac{\mu}{2\pi}\Delta V = \frac{a^3}{2}\Delta P \tag{2.3}$$

where a is the radius of the source. As confirmed by the inspection of the analytical solutions in Sasai (1991), the COP model does not depend on the rigidity modulus, whereas the COD model is linearly related to it. While in the COP model the piezomagnetic field is dependent on the intensity of the pressure applied at the source wall, in the COD model the piezomagnetic field is lower for a softer medium and higher for a stiffer medium. To assess the differences between COD and COP models in heterogeneous elastic medium, we computed the model B also for a COD model having the same volume increase as the COP model (Fig. 2.2a). The comparison between the COD and COP models shows significantly different results, indicating that the COD model is more sensitive to the elastic rheology (Fig. 2.2b). These results are in agreement with those obtained by Okubo and Oshiman (2004) who using a COD model noted significant

changes in the piezomagnetic field when boundaries of elastic layers are near to the source. The stress change in the COD model, and thus the piezomagnetic change, is strongly influenced by the elastic parameters. While the heterogeneity slightly affects the model in which the pressure change is assigned, it alters the solution when a volume change of the source is considered. Whether an intrusion process is better described in terms of a pressure source or of a volume change probably depends on the rheology of the medium. However, it is worth noting that for an elastic rheology a growth of magma chamber is better described in terms of pressure change than volume change, since the volume increase is indeed the resulting effect of source pressurization.

2.1.2 Effects of magnetic heterogeneity

Successively, models with heterogeneous distribution of initial magnetization, but homogeneous in elastic properties were also investigated (models C and D). Generally, in a volcano such as Etna, built up by a stack of basic lavas, magnetizations are irregular and frequently high (Hildenbrand et al. 1993). The magnetic properties of volcanic rocks cropping out in the Etna volcano have rarely been measured; however the few laboratory measurements carried out on recent and historic lava flows confirmed high values of remanent magnetization (J_{NRM}) ranging between 9.4 and 1. 4 A/m (Pozzi, 1977; Tanguy, 1975; Tric et al., 1994). Direct measurements of magnetic

properties of the most representative outcrops of the lower eastern side of Mt Etna, recently collected from lava flows and dikes, revealed an average J_{NRM} of 7 A/m with the highest values associated to dikes, while the lower ones related to volcaniclastic deposits (Del Negro and Napoli, 2002). Therefore, we assumed a high magnetization value for the volcano edifice lying on a substrate with lower magnetization. In particular, we considered two half-spaces with different layers and magnetic properties, thereafter referred as J_A and J_B (Fig. 2.3).

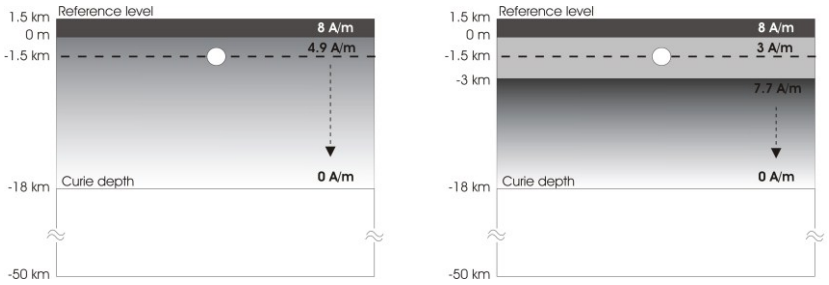

Figure 2.3 – Layered structures of the initial magnetization free from stresses. On the left the J_A two-layered magnetization structure, on the right the J_B three-layered magnetization structure.

Lateral heterogeneities are disregarded since they are poorly known and could alter the solutions. In the two-layered half-space J_A, we assume a value of the initial magnetization free from stresses J_o=8 A/m from ground surface to 0 m asl, reproducing the magnetization of the rocks in the volcano edifice. A lower value of J_o=5 A/m is considered in the layer from 0 to 18 km bsl that is the assumed Curie depth. It is reasonable to suppose a decrease in magnetization with

depth due both to the presence of areas with temperatures greater than Curie temperature and hydrothermal alteration occurring in zones surrounding magma storage or emplacement. Depth dependence is used to explain the loss of initial magnetization associated with the geothermal gradient, given by the following equation in SI units (Zlotnicki and Cornet, 1986; Stacey and Banerjee, 1974):

$$J = \begin{cases} J_0 \sqrt{1 - \left[(0.03(z_0 - z) + 10)/T_c\right]^2} & z_0 - z \geq \dfrac{T_c - 10}{0.03} \\ 0 & z_0 - z < \dfrac{T_c - 10}{0.03} \end{cases} \qquad (2.4)$$

where T_c=590 °C is the Curie temperature in degree Celsius, 0.03 °C/m the geothermal gradient, 10 °C the temperature at ground surface, z_0=1500 m the reference level and z is the depth in meters.

The simple two-layered model J_A, is an over-simplification of the variation of magnetization in the Etna subsurface. However, the intensity of magnetization can vary widely within volcanic edifice, because of changes in composition, grain size, and concentration of magnetic minerals (Rosenbaum, 1993). Considering the tomographic modelling of Etna plumbing system obtained by Chiarabba et al. (2000) and the geology-based models by Tibaldi and Groppelli (2002) (Fig.2.4), we also evaluated a three-layered half-space structure J_B.

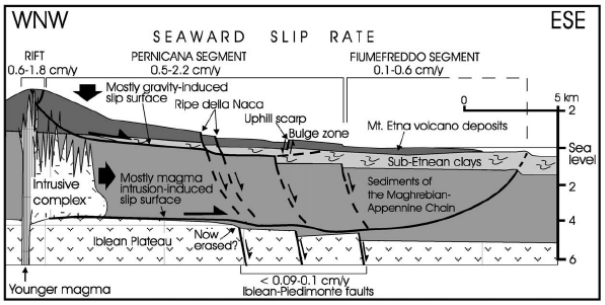

Figure 2.4 - Geological based model of Mt Etna by Tibaldi and Groppelli.

The first layer is the same as for the structure J_A. The second layer extends from 0 to 3 km bsl depth with a magnetization value of J_o=3 A/m. This lower value of J_o was speculated because of the presence of the regional apenninic structure, composed mainly of sedimentary rocks, surrounding and hosting the main intrusive bodies, and crystalline and metamorphic basement. Moreover, this layer is generally interpreted as the region where the magma is preferentially stored before the recent eruptions (Budetta et al, 2004; Bonaccorso and Davis, 2004; Bonforte et al., 2008). Here, the magma accumulation laterally extends for about 10 km, but the presence of hot fluids circulating around the shallow magma reservoir produce high values of temperature in a larger area (De Gori et al., 2005). The magnetization of the third layer, which starts from 3 km bsl, is assumed depth dependent following the Eq. (2.4). To this layer we associated an initial magnetization of J_o=8 A/m due to the presence of old intrusions that fed the past activity of volcano, fractionated by the magma during its uprising, stocked and congealed at depth.

The results of the models (C and D) with heterogeneity in

magnetization show that the shape of the variation is strongly dependent on the assumed magnetic structures (Fig. 2.5).

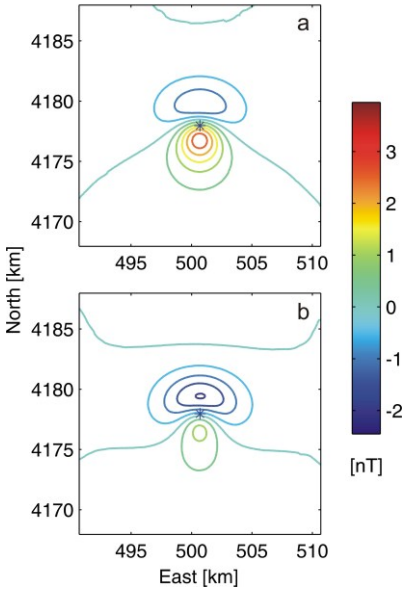

Figure 2.5 – The total piezomagnetic field for the half-space models C (a) and D (b). Contour lines are at 0.5 nT intervals.

In the heterogeneous model D both the shape and the amplitude of the expected magnetic field are perturbed (Fig. 2.5b). The comparison with the analytical solutions (Fig. 1.4) shows that the maximum values of the positive piezomagnetic changes reach 2.8 nT and 1.2 nT for the models C and D, respectively. Indeed, the piezomagnetic changes depend almost entirely on the stress-induced magnetization of the medium surrounding the source (Davis, 1976). In the heterogeneous model C the pressure source is surrounded by an average magnetization which is almost equal to that of model A and the

piezomagnetic variation does not change significantly. On the contrary, in model D a lower initial magnetization (3 A/m) is assumed around the source and a decrease in the piezomagnetic field is observed at ground surface with respect to the homogeneous model (A). A difference of about 1.5 nT in the negative polarity of the magnetic field is observed in the model D, where the amplitude of the negative polarity exceeds that of the positive one.

Both elastic and magnetization heterogeneities are then included in the models E and F with magnetization layers J_A and J_B, respectively (Fig. 2.6).

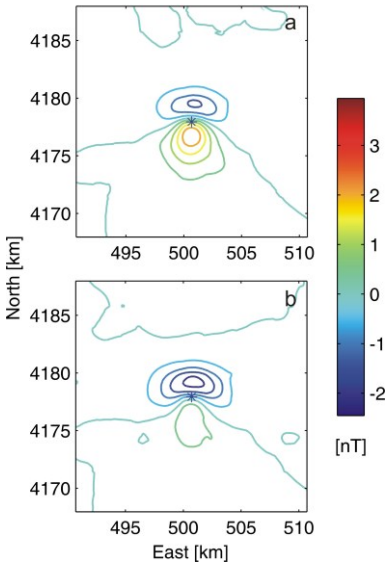

Figure 2.6 – Total intensity of piezomagnetic field (contour lines at 0.5 nT intervals) for the half-space models E (a) and F (b).

The elastic heterogeneities do not produce any significant variation in

the amplitude of the piezomagnetic field with respect to the elastic homogeneous models C and D. Only the shape shows small changes, just as occurred in the elastic heterogeneous model B.

2.2 Topography effect

To estimate the effect of topography on piezomagnetic fields, we included the real topography of Mt Etna in the previous models. The ground surface was generated using a digital elevation model of Mt Etna from the 90 m Shuttle Radar Topography Mission (SRTM) data and a bathymetry model from the GEBCO database (http://www.gebco.net/) (Fig.2.7).

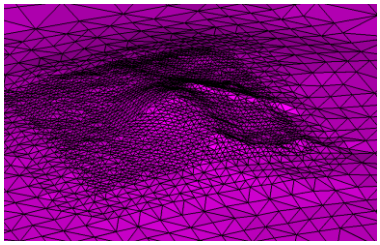

Figure 2.7 - Mesh of the topography of Mt Etna.

The computational domain was meshed into 152,859 isoparametric, and arbitrarily distorted tetrahedral elements connected by 26,090 nodes.

The medium is initially assumed to be homogeneous in elastic and magnetic properties in order to estimate the differences due to the topography separately. A change in shape is clearly observed in the

proximity of the volcano summit, where a sharper decrease is obtained with respect to the analytical solution (Fig. 2.8).

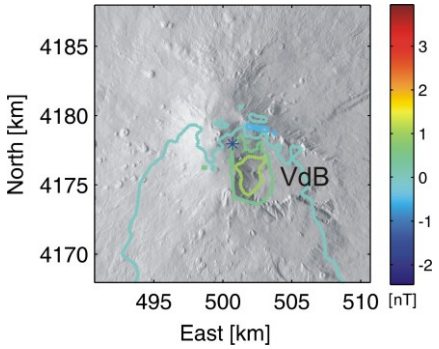

Figure 2.8 – The magnetic field changes for a homogeneous magneto-elastic medium with the real topography of Mt Etna. Contour lines are at 0.5 nT.

The piezomagnetic changes do not exceed 1.5 nT with a decrease of about 1.5 nT in comparison with the half-space model A. Significant differences are observed in the summit area where the relative distance between the ground surface and source position is increased. The solution is mainly influenced by the rugged topography and the steepest relief in the depression of the Valle del Bove (VdB) on the east flank of Etna. The presence of the depression alters the shape of the piezomagnetic field. The symmetry of the magnetic components and total magnetic intensity in the half-space homogeneous model is lost in the numerical results, since the volcano edifice is rather asymmetric and has a mass deficit in the eastern sector. The variation seems to be delimited by the cliffs of the Valle del Bove and its maximum slightly moved toward south-east.

Following the same procedure for the multilayered models, topography and heterogeneity features in elastic parameters and initial magnetization (models E and F, see Table 2.1) are simultaneously accounted for. In particular, the amplitude reaches the value of 1.3 nT and 0.5 nT for the structure J_A and J_B, respectively. The shape of the solution is similar to that of half-space models E and F (Fig. 2.9), but it is very irregular because of the topography effect (Fig. 2.9).

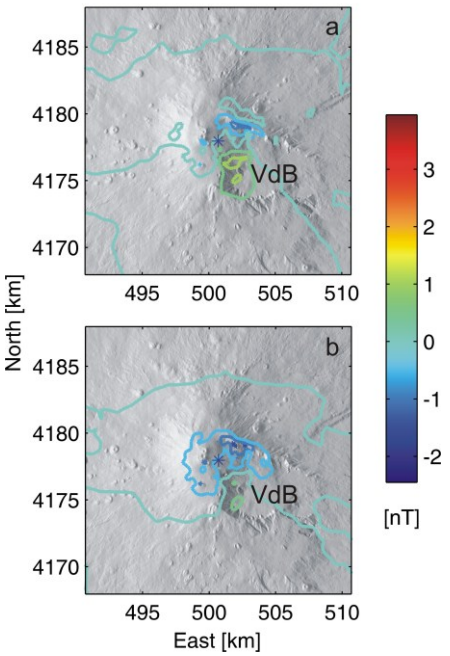

Figure 2.9 – Total intensity of piezomagnetic field for the models E (a) and F (b) with the real topography of Mt Etna. Contour lines are at 0.5 nT intervals.

Also in this case, the numerical solutions for model F highlight a decrease in the maximum value of the piezomagnetic field, because the initial magnetization around the source is lower than that of the

homogenous model (A). It is worth noting that for the structure J_A the minimum follows the northern cliff of the Valle del Bove, while in J_B it extends significantly westwards going beyond the summit craters. This could be related to the strong magnetization contrasts between different layers.

2.3 Discussions

In this section we examined the effects caused by medium heterogeneities and real topography on piezomagnetic field for a pressure source.

Our findings highlight that heterogeneity and topography engender deviations from analytical results in the piezomagnetic fields produced by pressurized sources under elastic conditions. In a heterogeneous elastic medium, differences between piezomagnetic fields produced by a pressure change and a volume change within a spherical source are obtained, evidencing the greater sensitivity to the elastic rheology when a volume change is assigned to the source. In this case, the stress field, and in turn the piezomagnetic change, is lower for a softer medium and higher for a stiffer medium. The piezomagnetic field changes are highly dependent on the assumed magnetic structures. Although the magnetic features of Etna volcano are not well known, we investigated two different layered half-spaces, J_A and J_B, with different magnetic properties. It is worth noting that piezomagnetic change related to J_A, which has little magnetization contrast, is very

similar to the homogeneous model, while the strongest magnetization contrasts of J_B produce an unexpected variation. This supports the idea that a better knowledge of magnetization distribution inside the volcanic edifice is essential to improve numerical models. On the other hand the elastic heterogeneity, which was estimated from seismic tomography, only slightly affects the amplitude of the piezomagnetic field (at least for a COP source).

The actual 3D topography also affects the generation of piezomagnetic field changes because of stress concentration effect near the rugged ground surface. In particular, the Valle del Bove, with its steep cliffs, perturbs the shape of the field whose maximum is well confined inside it, while the minimum follows the northern rim of this depression.

The location of our pressure source is similar to that of the sources involved in the flank eruptions occurring during the 2004-2006 period (Bonforte et al. 2008). In agreement with the numerical results, no significant magnetic variations were detected by the Etna permanent magnetic network in this period, because stations are located outside the Valle del Bove depression (Napoli et al., 2008). Moreover, the expected piezomagnetic field is strongly influenced by the magnetization properties of the rocks surrounding the pressure source. If the source is located within the lower magnetic layer, negligible piezomagnetic variations will be generated. On the other hand, higher piezomagnetic field changes are expected due to magmatic intrusions within the volcanic edifice characterized by high rock magnetization,

as observed during the last Etna eruptive events (Del Negro and Currenti, 2003; Del Negro et al., 2004; Napoli et al., 2008).

Our results evidenced that strong perturbations of the piezomagnetic field are more evident in presence of severe heterogeneities and steeper topography, i.e. at the volcano summit. It is evident that the analytical model overestimates the expected magnetic changes. Standard analytical models, that neglect the complexities associated with morphology and medium properties of volcanic edifice, could provide an inaccurate estimate of the expected geophysical changes and, hence, lead to a misinterpretation of source parameters in inverse problems. The application of FEMs, instead, allows for more accurate interpretations and inferences in modeling-based assessments of geophysical changes associated with volcanic activity providing more reliable insights into volcanic source definition.

Chapter 3

Application to Real Case Studies at Etna Volcano

Mt Etna is one of the better monitored and successfully studied volcanoes in the world, where continuously running magnetic, gravity and geodetic networks are operating (Bonaccorso et al. 2004). Since 1988 a dense GPS network consisting of about seventy benchmarks is measured periodically (Bonforte et al 2008).

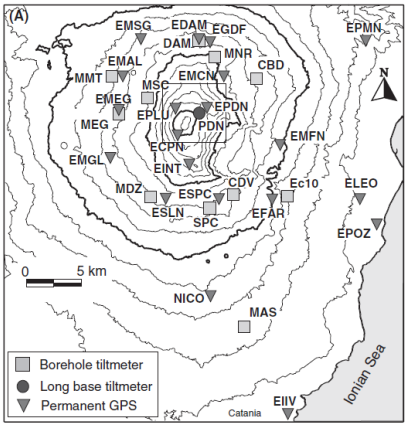

Fig. 3.1 - Continuous GPS monitoring network at Mt Etna

Gravity and magnetic monitoring systems running at Etna were set up in 1998 and improved during recent years (Del Negro et al. 2002; Del Negro et al., 2004). Gravity continuous observations are integrated by discrete measurements that are regularly gathered over an area of about 400 km^2 (Fig. 3.2).

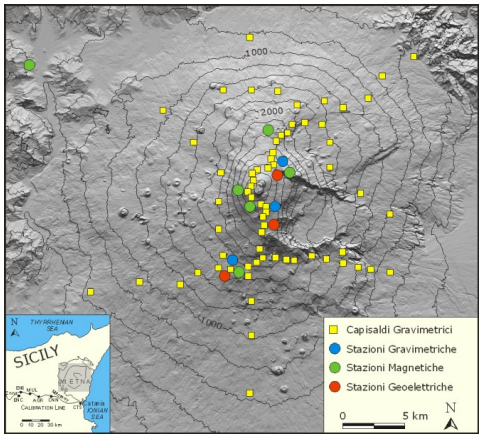

Fig.3.2 - Gravity and magnetic monitoring networks at Mt Etna.

The amount of available data collected represents a valuable database, but up to date limited efforts have been made for an effective integration of different data.

To validate the goodness of the integrated numerical model described in the previous chapter, we applied it to two different cases study to simultaneously calculate deformation, gravity and magnetic field and to provide a realistic model that explains the observations carried out on Mt Etna in 2005-2006 inflation period (Bonforte et al., 2008) and during the magmatic intrusion occurred on 13th May 2008 on the northern flank of the volcano (Napoli et al., 2008). These two case studies are representative of the different nature of the volcanic sources, that are pressure source and intrusive sources.

The two kinds of activities of Mt Etna offer an exemplary case study to validate the capability of the integrated numerical model, proposed in the previous chapter. We applied the numerical model to explain the geophysical changes observed in occasion of the intrusive process occurring in the northern flank of the volcano (Napoli et al., 2008; Aloisi et al., 2009) and the inflation process due to pressurizing magma (Bonforte at al., 2008). Even if the analytical models provide an acceptable representation of the magma processes, they do not explain the observed geophysical variations in details because a simple elastic half-space assumption is used. Therefore, we review the analytical models by constructing a 3D numerical model including the real topography of the Etna and the magneto-elastic heterogeneity to

jointly evaluate ground deformation, magnetic and gravity changes caused by the magmatic processes.

3.1 Numerical model of Mt Etna

A fully three-dimensional elastic finite element model of Mt Etna was designed, accounting for topography and medium heterogeneity, which can alter the estimate of the investigated geophysical changes. We solve the model equations as described in the previous chapter.

The real 3 D topography of Mt Etna, which is rather asymmetric with a prominent mass deficit in correspondence of Valle del Bove, was taken into account (Fig. 2.15).

Heterogeneous distribution of magneto-elastic properties is included in the model (Fig. 3.3). Considering the tomographic image of Etna plumbing system obtained by Chiarabba et al. (2000) and the geological models by Tibaldi and Groppelli (2002), we evaluate a three-layered half-space structure. For the first layer, that extends from ground surface to 1 km asl, we assume a value of Young modulus of 17 GPa, reproducing the low rigidity of the rocks in the volcano edifice. For the second layer, from 1 km asl to 4 km bsl, we assume a value of 40 GPa that represents the rigidity of a sublayer with different properties. Finally, the third layer, which extends from 4 km bsl to the bottom of the domain, is supposed with a higher rigidity with value of 80 GPa. The Poisson's ratio is assumed homogeneous in the entire domain and has a value of 0.25. We do not

include heterogeneity in the rock density properties since density models available at Etna have low resolution and accuracy (Corsaro and Pompilio, 2004; Schiavone and Loddo, 2007), especially at shallow depth where the intrusion occurred. To estimate the gravity changes, we hypothesize a medium with homogeneous density ρ_c=2500 kg/m^3. Heterogeneous distribution of initial magnetization is also used in the piezomagnetic model. We assume a value of the initial magnetization free from stress J_o=8 A/m from ground surface to 1 km asl, reproducing the magnetization of the rocks in the volcano edifice (Currenti et al., 2009). The second layer starts with a initial magnetization value of J_o=5 A/m that decreases in depth with the geothermal gradient until reaching the depth of the Curie isotherm (TC ≈550°C for Etna's rocks) at about 18 km (Currenti et al., 2009).

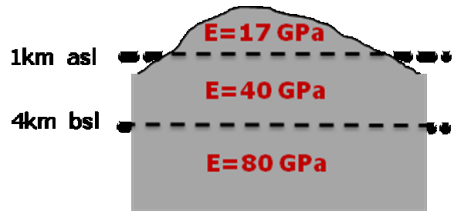

(a)

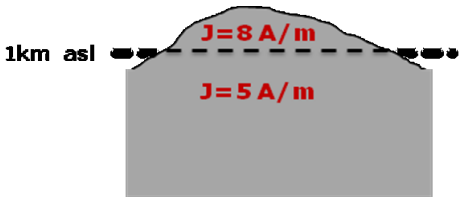

(b)

Fig. 3.3 - Distribution of Young Modulus (a) and rock magnetization (b) in numerical model of Mt Etna.

3.2 Pressure source model: 2005-2006 Etna activity

The 2006 eruption of Mt Etna, occurring from July to December, was characterized by episodic eruptive activity involving a number of explosive and effusive vents in the summit areas. Volcanic activity started at summit craters of the volcano on 14 July 2006, when a fissure opened on the east flank of the South-East Crater (SEC) producing a lava flow spreading east to the Valle del Bove and moderate strombolian activity. This eruptive phase ended on 23 July, and was followed by strombolian activity at the North-East Crater (NEC) and at SEC (Neri et al 2006) during the summer. Episodic eruptive activity continued until December 2006. Similarly to the latest flank eruption of 2004-05 (Burton et al., 2005), no geophysical precursors, such as seismic swarms, volcanic tremor and ground deformation, were observed prior to the onset of 2006 eruption, which started as a passive flank effusion accompanied only by a slow and constant increasing in the volcanic tremor amplitude.

Since the end of 2005, Mt. Etna has generated quasi continuous magnetic activity, even when no significant eruptive activity was observed. In Figure 3.4 the daily means of total intensity variations in the period 2005-2006 observed at CSTs, CSTn, BVD, BCN, PDN, PDGs, PDGn and DGL, relative to CSR are shown. Magnetic field measurements are usually differentiated with respect to the reference station to isolate local magnetic field changes and cancel out common noise from ionospheric and magnetospheric sources and filtered by a simple one-coefficient filter (Del Negro and Currenti, 2003) to remove

periodic fluctuations correlated with seasonal temperature variations. After processing, a slow and continuous decrease in the magnetic field total intensity was observed at CSTs, CSTn and BVD located on the southern flank of the volcano. The total amount of the decrease during the 16-month period is 12 nT and 11 nT respectively at BVD and CST. During the same period BCN and PDN show a regular increase of about 5 nT. The amount of the decrease falls off northward and no significant variations are observed at PDG and DGL.

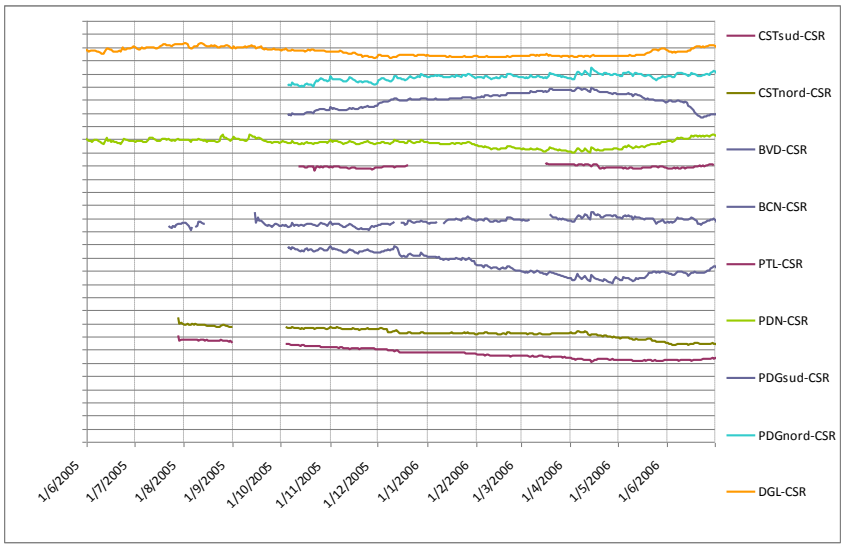

Fig.3.4 - Magnetic measurements at Mt Etna during the period 2005-2006

Gravity field during 2005-2006 shows a decrease in the summit station; once the measured values have been corrected for the "free air" effect, due to significant changes in the elevation of the measurement point with respect to the centre of gravity of the Earth,

the observations are still characterized by a negative anomaly in all the summit area of volcano (Fig. 3.5).

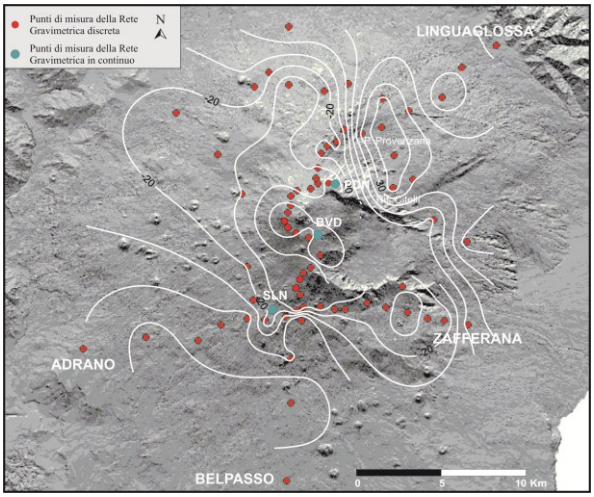

Fig. 3.5 - Gravity anomaly observed at Mt Etna during the period 2005-2006. Contour lines are at 10 μGal.

Deformation field recorded on Mt. Etna in the same period evidenced a recharging phase when the volcano began to inflate, showing an opposite ground deformation pattern to that detected for the previous year. Recently, Bonforte et al. (2008) modeled the 2005-2006 GPS data by a pressurized near-vertical prolate ellipsoid elongated source located beneath the summit craters at a depth of ~3.5 km below sea level and a sliding plane that models the southeastward motion of the eastern flank (Fig. 3.6).

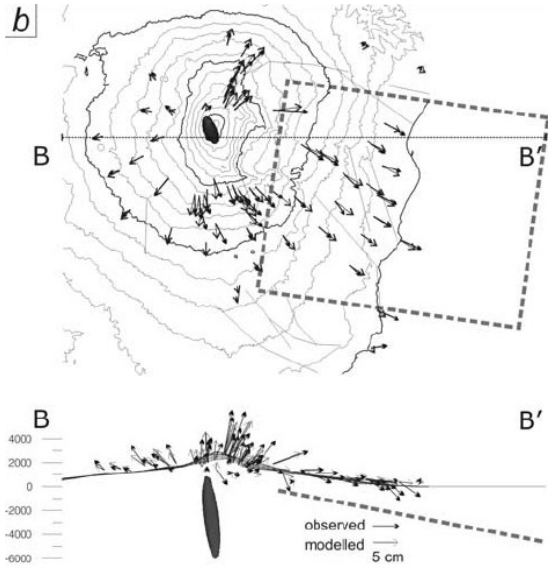

Fig. 3.6 - Source modeled by Bonforte et al. (2008) represented by an ellipsoidal pressure source and a sliding plane, together with the comparison between the observed and the modelled ground deformation vectors.

Here we estimated the geophysical changes expected to accompany the 2005-2006 inflation episode on Mt Etna applying the ellipsoidal source model by Bonforte et al. (2008). We calculate deformation, gravity and magnetic change on surface due to the ellipsoidal source described above (medium and source parameters are showed in Table 3.1), disregarding the effect of the sliding plane to model only the summit phenomena.

Table 3.1- Source geometry and medium properties by Bonforte et al. (2008).

Model Parameters	Value
Curie Depth	18000 m bsl
Magnetic Inclination	51°
Magnetic Declination	1°
Stress Sensitivity	0.0001 bar^{-1}
Density Medium	2500 kg/m^3
ΔP (MPa)	60
1^ Euler angle (Vert to c-axis)	-94.68°
2^ Euler angle (North to a-axis)	-36.67°
3^ Euler angle (rotation a on perp c-axis)	107.17°
b/a	0.2
c/a	0.16
Xc	499096 m
Yc	4177864 m
Depth	3692 m

We would like to emphasize that we do not invert either the geodetic data or the magnetic and gravity data but we assume the ellipsoidal source (at 3.5 km b.s.l. depth) retrieved by Bonforte et al. (2008) to compute the expected geophysical changes. Obviously, quantitative models cannot purport to cover all different physical and chemical aspects of volcanoes; it is important to select and focus on the key phenomena, that is in this case the inflation pattern in summit area of volcano.

The computational domain was meshed into 146207 isoparametric, and arbitrarily distorted tetrahedral elements connected by 25146 nodes (Fig. 3.7).

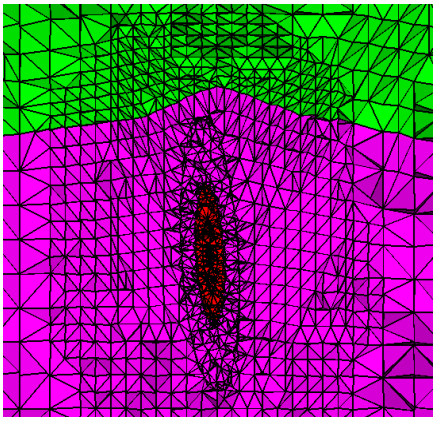

Fig.3.7 - Section of the mesh of the computational domain.

Geophysical changes obtained with numerical model are consistent with the observation for amplitude, sign and shape, indicating that, even if the model is a simplified version of the scenario of Mt. Etna, it can reproduce the principal effects that characterized the 2005-2006 inflation phase.

The comparison between the observed and the expected displacement vectors, reported in Fig. 3.8, shows that the ground deformation pattern of the 2005–2006 dilating phase can be well modelled with the source model by Bonforte et al. (2008).

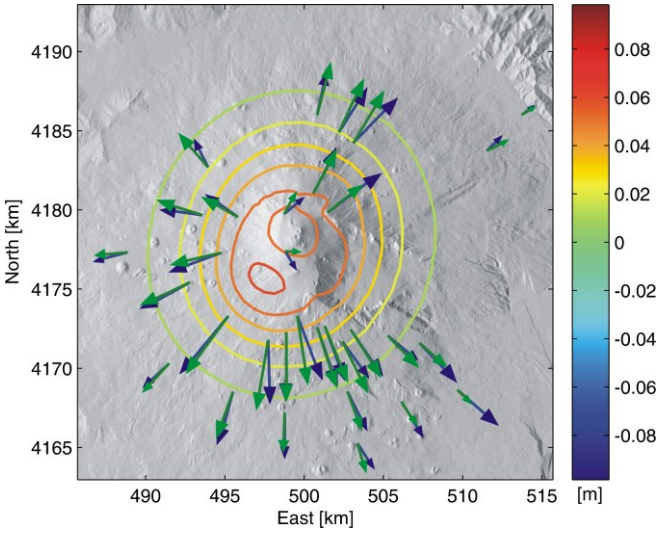

Figure 3.8 – Comparison between deformation field observed at the GPS stations at Mt. Etna (blue arrows) and computed deformation field generated by the pressure source (green arrows). Contour lines (at 1 cm intervals) represent the vertical displacement anomaly computed with the numerical model.

In Fig. 3.9 and 3.10 we report the computed piezomagnetic and thermomagnetic changes produced by the pressurized source modeled by Bonforte et al., 2008. The amplitude, time-scale and polarity of magnetic observations on surface lead to interpret the thermomagnetic phenomena as the primary mechanism generating magnetic anomaly; piezomagnetic effect is also taken into account but it could be neglected with respect to the thermomagnetic effect. In Fig. 3.10 the comparison between the observed magnetic field and the computed thermomagnetic field is reported. The pattern of numerical results well fit with observations, especially in polarity of magnetic field:

piezomagnetic (Fig. 3.9) and thermomagnetic (Fig. 3.10) field are computed by numerical model, the first resulting in a negative intensity of magnetic field at North and positive at South, the second in an inverse polarity. Numerical simulations show that thermomagnetic effect is dominant, according to the sign of the observed anomaly. Only local effect could have produced discrepancies between expected and observed data, for example at BCN station.

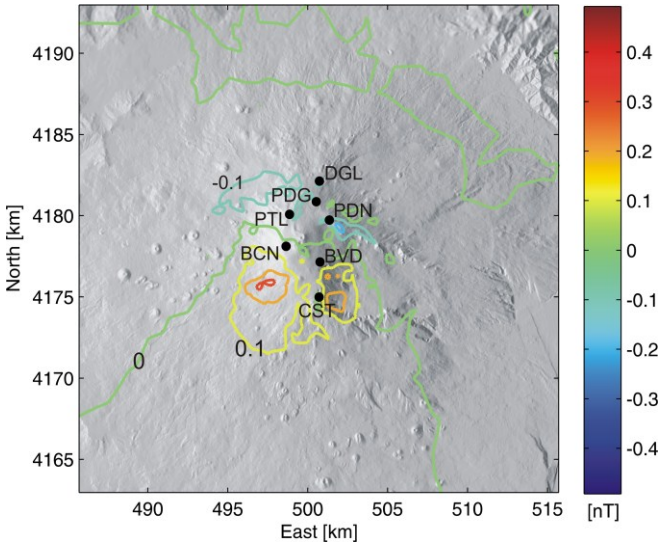

Figure 3.9 – Piezomagnetic anomaly (contour lines at 0.1nT) generated by the pressure source. The black circles are the magnetic stations of monitoring network at Mt. Etna.

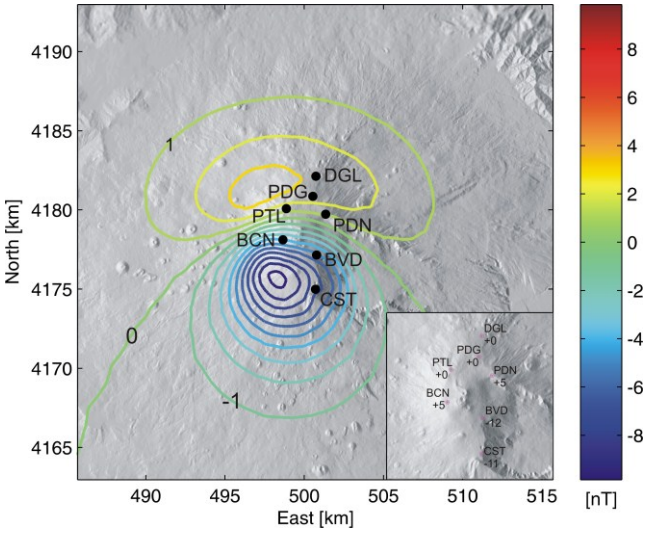

Figure 3.10 – Thermomagnetic anomaly (contour lines at 1nT) generated by the pressure source. The black circles are the magnetic stations of monitoring network at Mt. Etna. Inset shows the magnetic variations observed at the monitoring stations.

In gravity model we suppose a medium with homogeneous density ρ_c=2500 kg/m^3, a magmatic source with a density before the inflation ρ_m=2600 kg/m^3 and after the inflation ρ_m'=2550 kg/m^3. The value of ρ_m' is chosen minimizing the misfit between observed and expected results. The hypothesis of ρ_m'<ρ_m indicates that a mass intrusion with high gas concentration could have occurred at depth to justify both ground deformation and gravity observations. If the ellipsoidal source was inflated with no addition of new mass, the overall gravity contributions should have leaded to a negative gravity anomaly that was not sufficient to justify the observations. However a mass intrusion with high gas concentration could have occurred, whose

effect increased the negative contribution given by the other terms. We can infer the mass change of $-15*10^{10}$ kg inside the ellipsoid source in a way to justify the gravity observations.

Observations of gravity field, corrected for "free air" effect, reported in Table 3.1, are characterized by a negative anomaly centred at West with respect to summit craters, that well fits with pattern of numerical result (Fig. 3.11), even if local effects and measurement errors (about 15 μGal) lead to localized discrepancies between expected and measured data, resulting in a standard deviation of residual of 12.2 μGal**.** (Tab. 3.2), that is below the threshold of the measurement error.

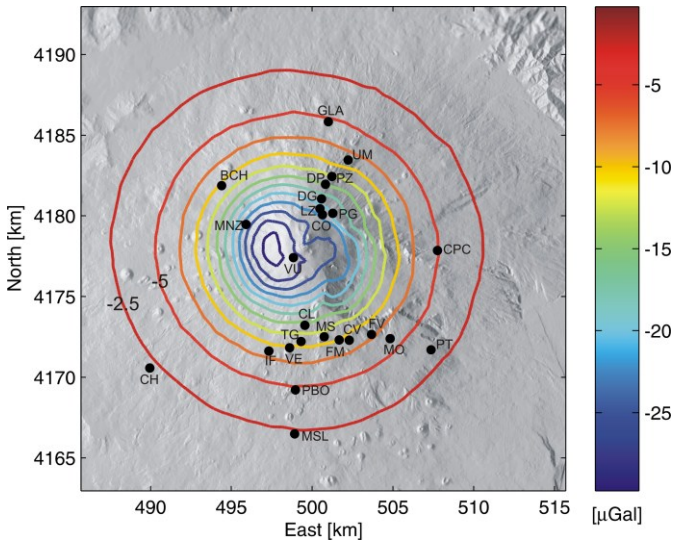

Figure 3.11 – Gravity anomaly (contour lines at 2.5μGal) generated by the pressure source. The black circles are the gravity stations of monitoring network at Mt. Etna.

Tab.3.2 - Gravity variations related to 2005-2006 period observed at the monitoring stations at Mt. Etna after having been corrected for free air effect.

Station	Longitude (m)	Latitude (m)	Gravity Data (μGal)
PBO	498964	4169218	-11
VU	498836	4177411	-49
GLA	500999	4185838	-25
PT	507360	4171703	-19
BCH	494398	4181870	-28
CPC	507756	4177851	-2
IF	497327	4171625	-8
MO	504824	4172388	-16
VE	498612	4171824	0
TG	499320	4172213	-24
MS	500747	4172507	-29
FM	501677	4172309	-8
CV	502294	4172298	-10
FV	503677	4172650	-24
UM	502224	4183460	0
PZ	501223	4182432	0
DP	500826	4181964	-17
DG	500585	4181057	-33
LZ	500484	4180442	-5
CO	500638	4180072	-3
CL	499547	4173220	-25
MNZ	495914	4179465	-19
PG	501279	4180155	-23

Our findings highlighted two main points. First, the source modelled by Bonforte et al. (2008) is able to explain the pattern of the observed magnetic and gravity changes, evidencing that all geophysical changes, that independently reflect the state of the volcano but are ascribed to the same volcanic source, have to be modelled jointly. Second, the application of FEMs allows for accurate interpretations

and inferences in modeling-based assessments of ground deformations, gravity and magnetic changes associated with volcanic activity providing more reliable insights into volcanic source definition with respect to analytical modeling.

3.3 Intrusive source model: 2008 Etna Eruption

The onset of the 2008-2009 eruptive activity was accompanied by a superficial seismic swarm taking place in a NNW-SSE elongated area at the eastern base of Mt Etna summit craters. On 13th May 2008, epicenters time patterns evidenced an almost stationary distribution in the upper flanks of the Valle del Bove until 9:30 GMT, then a clear migration of the seismic events occurred toward the top of the North-East Rift, suggesting a northward propagation of a magmatic intrusion. Earthquakes were accompanied by a gradual and intense increase in the intensity of volcanic tremor (Di Grazia et al., 2009). The volcanic activity was characterized by the opening of a fracture field on the northern flank of the volcano (Fig. 3.12), and an E-W eruptive fissure in the upper sides of the Valle del Bove (Napoli et al., 2008; Aloisi et al., 2009).

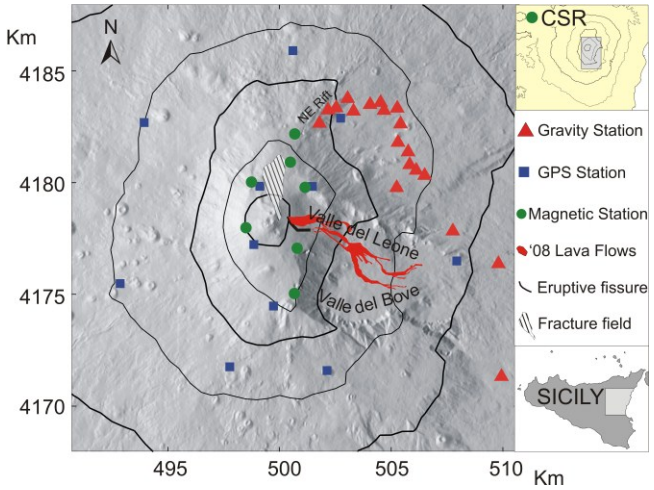

Figure 3.12 – Schematic map of the Etna summit area covered by the lava flows of the 2008 eruption. Locations of magnetic, gravity and GPS stations are also shown. Inset shows the position of the CSR magnetic reference station.

Remarkable changes in the local magnetic field were observed in coincidence with the seismic swarm onset. No significant variations were observed before 13th May, while large negative changes in local magnetic field (the amplitude ranges between -1.8 and -6.5 nT) occurred at the stations placed on the northern flank of the volcano within a few hours coinciding with the quick epicentral migration of the seismic events from Valle del Bove toward the North-East Rift (Napoli et al., 2008), as showed in Fig. 3.13.

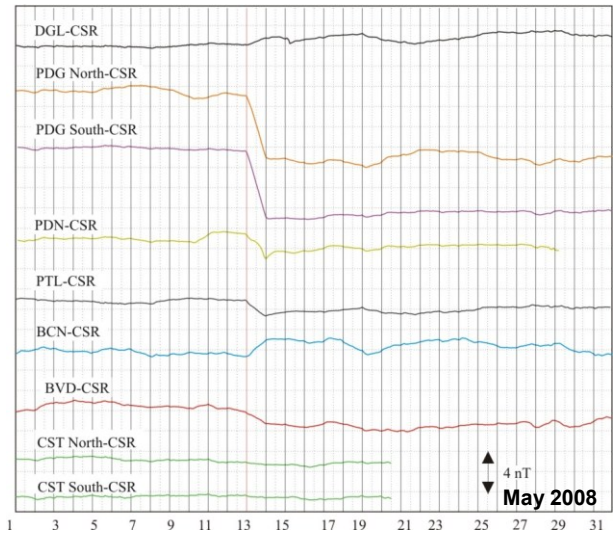

Figure 3.13 - Magnetic observation at the magnetic stations during the 2008 eruption at Mt Etna.

Discrete gravity measurements were carried out at 19 benchmarks along a profile that lies between 500 and 2200 m a.s.l. of altitude on the north-eastern flank of the volcano. Measurements gathered on 14th May 2008 were referenced to the gravity survey performed on 5th May, but no significant variations were observed (Budetta et al., 2008).

Remarkable ground deformation was recorded by permanent tilt and GPS networks. Changes started first in the summit area where the largest variations (about 100 μrad) were detected, and successively were observed in the middle flanks of the volcano but with much smaller amplitudes. The summit stations of the continuously recording GPS network detected horizontal displacements of a few tens of

centimetres (Fig. 3.14 from Aloisi et al, 2009). Smaller variations of a few centimetres were detected at the other stations. The deformation pattern was radial with respect to the summit area (Aloisi et al., 2009).

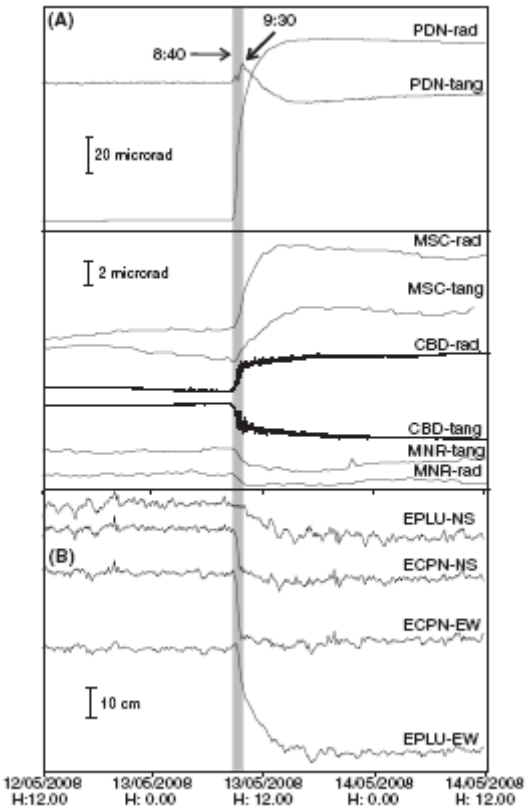

Figure 3.14 - (A) Radial (rad) and tangengential (tan) tilt components recorded during the 713 May 2008 intrusion. (B) Selected North–South (N–S) and East–West (E–W) position components recorded by the GPS network. The signals are smoothed using a mobile average with a 10-min duration window. The grey box indicates the first phase of the intrusion (Aloisi et al, 2009).

Preliminary analytical solutions were used to model the geophysical observations and infer the intrusion source parameters. Magnetic data inversion indicated the response to a tensile mechanism with an intrusion crossing the volcano edifice along a ca. NNW–SSE direction in the northern flank attributable to piezomagnetic effects. The estimated intrusive dike, located within the zone of the seismic swarm that occurred during magma propagation, engenders a deformation pattern that well fits also the ground deformation recorded by the continuous GPS network operating on Mt Etna. Gravity changes expected from the same intrusive dyke are below data uncertainty at the gravity benchmarks confirming a lack of significant variations in the investigated area (Napoli et al., 2008). Also geodetic data inversion evidenced a shallow intrusion propagating laterally to the NNW direction from the central conduit (Aloisi et al., 2009). In contrast, the E-W eruptive fissure in the Valle del Bove could have given only minor contribution to stress and strain changes probably because of the highly fractured and compliant rocks of this area. Indeed, magma intruded toward the Valle del Bove without any seismic events and lava effused almost passively (Napoli et al., 2008; Aloisi et al., 2009).

We applied the numerical model described in the previous chapter to compute geophysical changes associated with the magmatic intrusion. The computational domain was meshed into 215009 isoparametric, and arbitrarily distorted tetrahedral elements connected by 38007 nodes (Fig 3.15). The intrusion source is simulated as a discontinuity

surface by introducing the mesh nodes in pairs along the surface rupture.

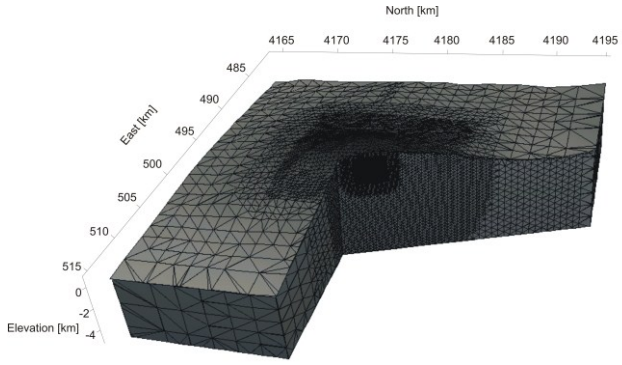

Figure 3.15 – View of the mesh of computational domain, with a high resolution in the areas near the source.

The preliminary numerical solution (model A) was obtained using the source geometry obtained by the analytical inversion model by Napoli et al. (2008). In this way we can appreciate how the heterogeneous distribution of magneto-elastic parameters in the medium and the topography make the numerical results differ from the simple analytical solutions from a homogeneous half-space model having an elastic rigidity μ = 30 GPa, Poisson ratio ν = 0.25 and density ρ = 2500 kg/m^3. It is worth noting that we do not invert either the geodetic data or the magnetic and gravity data, but we assume the intrusion source to estimate the expected geophysical changes. A dislocation model was simulated assigning an opening of 2 m along the discontinuity surface striking N 20° W, dipping 80° E, with a length of 2.5 km, width 2 km, representing the magma intrusion.

Numerical results (Fig. 3.16b) compared to analytical solutions (Fig. 3.16a) reveal slight differences in pattern and intensity of the deformation field at the summit GPS stations.

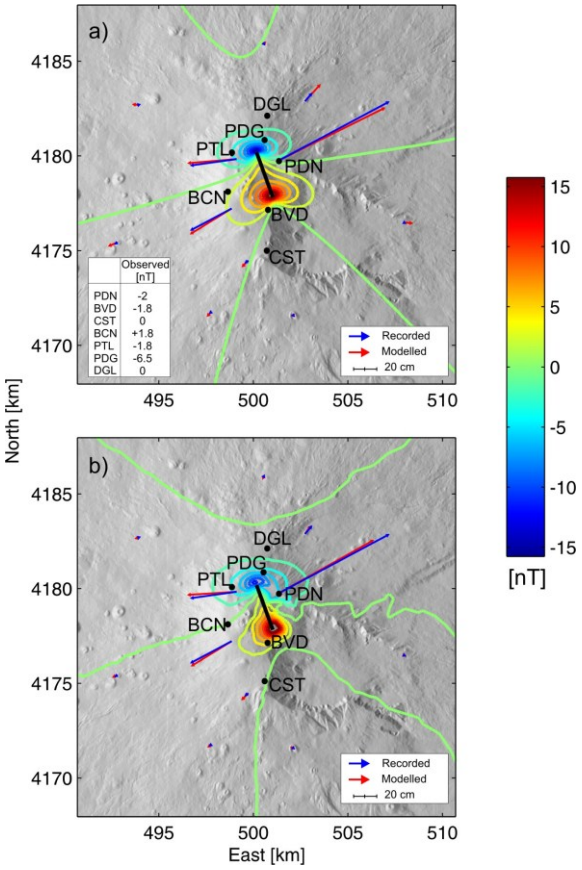

Figure 3.16 – Comparison between analytical solutions (a) and numerical results of model A (b) for the 2008 intrusive source from Napoli et al. [2008]. Piezomagnetic change (contour lines at 2 nT) generated by the intrusive dike (black line). Observed (blue arrows) and computed (red arrows) deformation at the permanent GPS stations are also reported. The recorded magnetic changes are reported in the inset.

However, stations located at lower altitude show a higher misfit with respect to the half-space homogeneous model. At mid-flank stations, where the role of topography is clearly very important, the horizontal deformation decreases and the match with the observations improves. In contrast, the piezomagnetic field changes show significant deviations from the homogeneous half-space solution. Significant discrepancies are observed at most of the magnetic stations (Fig. 3.17).

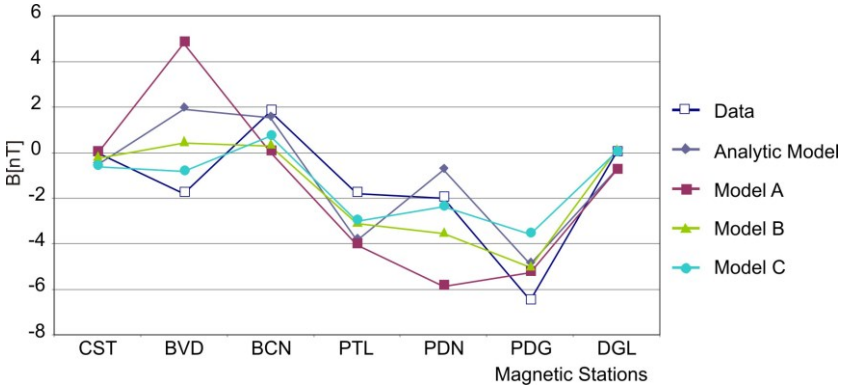

Figure 3.17 – Comparison between measured and computed magnetic changes for the analytical and numerical models.

The symmetry of total magnetic intensity observed in the analytical model is lost in the numerical result (Fig. 3.16b). The shape of the piezomagnetic field is strongly modified in the eastern sector of the volcano in correspondence with the rugged topography. The piezomagnetic field is wider and more intense than the analytical one in the northern flank, and significant discrepancies, up to 5 nT,

between the numerical and analytical models are observed at the magnetic stations (Fig. 3.17). In particular, the highest discrepancies are observed at BVD and PDN stations. In the numerical model the amplitude of the piezomagnetic field increases at BVD and PDN stations, while it decreases at BCN. Therefore, a higher misfit with respect to the magnetic observations is obtained in the numerical model A. Each contribution to the gravity field (see Eq. 2.15) was investigated separately using both the analytical (Okubo, 1992) and numerical solutions to understand their own effects (Figs. 3.18 and 3.19).

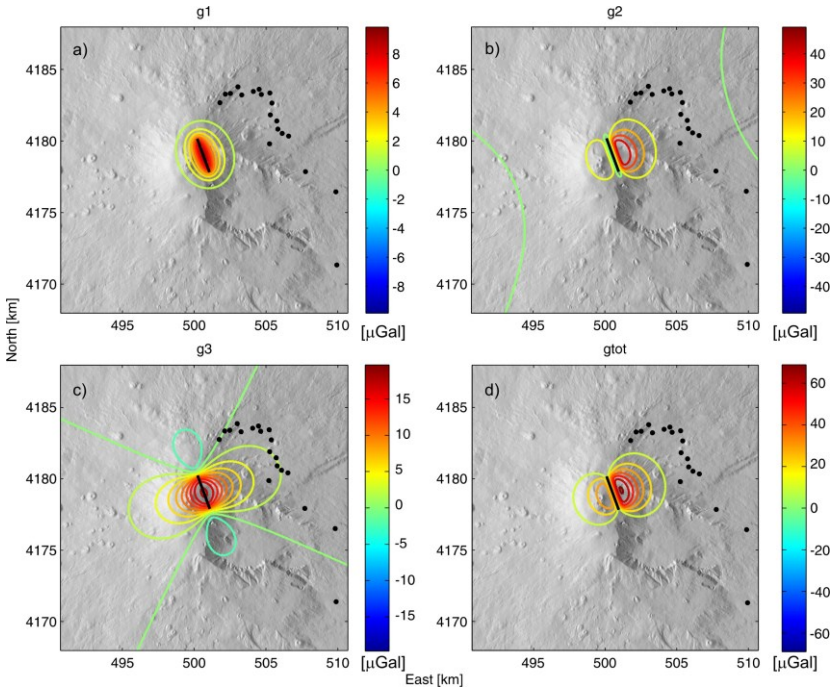

Figure 3.18 - Gravity contributions generated by the intrusive source using the analytical solution. Contour intervals are 1 μGal for δg_1 (a), 10 μGal for δg_2 (b), 2 μGal for δg_3 (c) and 10 μGal for the total gravity change (d). Black circles represent the gravity stations of the monitoring network at Mt. Etna.

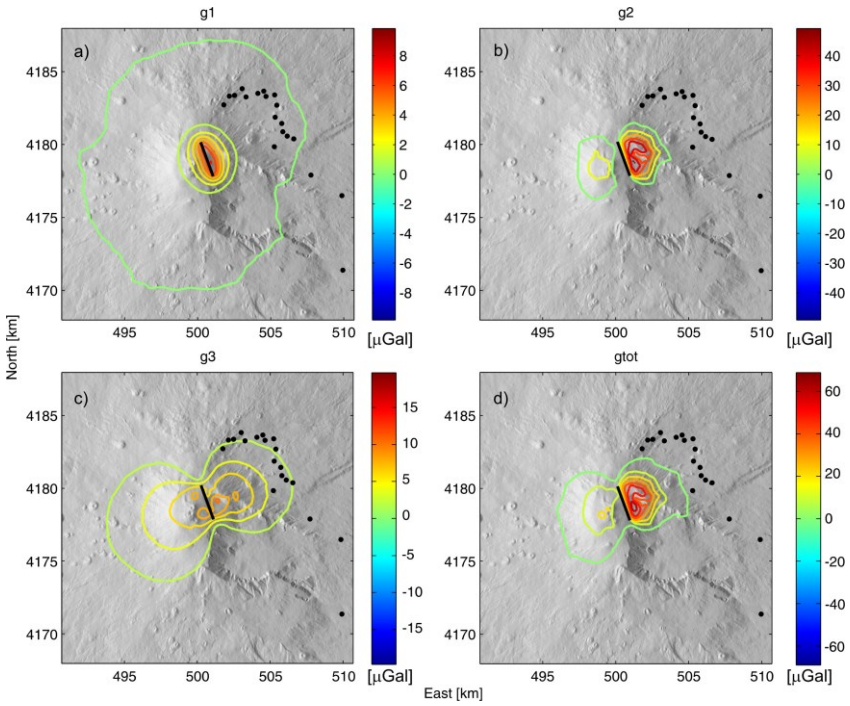

Figure 3.19 – Gravity contributions generated by the intrusive source using the numerical model A. Contour intervals are 1 μGal for δg_1 (a), 10 μGal for δg_2 (b), 2 μGal for δg_3 (c) and 10 μGal for the total gravity change (d). Black circles represent the stations of the gravity monitoring network at Mt. Etna.

Numerical solutions (Figs. 3.19), as well as the analytical ones (Figs. 3.18), show significant variations only in proximity of the magmatic

intrusion, where, unfortunately, no data are available. The predominant contribution is the δg_2 term, originating from the displacement of density boundaries at the ground surface (Figs. 3.18b and 3.19b). Even if a magmatic source with a density contrast of $\Delta\rho$=200 kg/m^3 is assumed, the δg_1 contribution (Figs. 3.18a and 3.19a) related to the mass intrusion attains an amplitude less than 10 μGal. This contribution is comparable with δg_3 (Figs. 3.18c and 3.19c) produced by dilation/contraction of the medium arising from finite compressibility of the material. In the analytical solution the δg_3 is about double than in the numerical model A, where rocks maybe do not contract as much as in the half-space domain because of the less constraining steep topography. The total gravity change (Figs. 3.18d and 3.19d) reaches a maximum amplitude of about 70 and 60 μGal for both the analytical and the numerical model A, respectively. Discrepancies between analytical and numerical solutions are negligible as regards the field intensity, while notable changes in the pattern are observed. The gravity change, indeed, is wider and is strongly modified mainly in the summit area and in the eastern flank of Etna. The gravity field extends about 3-4 km from the magma intrusion and does not show significant changes at the gravity benchmarks, where in agreement with the models no gravity variations were recorded.

Although changes in the gravity field are generally interpreted only in terms of additional mass input, our numerical results show that for a shallow magmatic intrusion the main contribution arises from the displacement of density boundaries. Moreover, the gravity changes

highlight a butterfly pattern that is strongly different from the expected concentric pattern coming from the contribution of a mass input alone.

The values of chi-square for deformation components and magnetic changes are calculated to quantify the fit with the observed geophysical changes (Table 3.3).

Table 3.3 - Chi-square values of deformation and magnetic changes for the analytical and the numerical models.

	Analytic Model	***Model A***	***Model B***	***Model C***	***Model D***
Magnetic	255	766	150	140	140
Horizontal deformation	426	396	405	1650	557
Vertical deformation	609	487	350	1200	423

The estimated measurement errors are 0.2 nT for the magnetic changes and 0.005 m and 0.05 m for the horizontal and vertical deformation, respectively (Napoli et al., 2008; Aloisi et al., 2009). To enhance the match between the data and the numerical solutions including topography and medium heterogeneity, we changed some source parameters. In particular, we reduced the width of the dike until numerical solutions better fit the observed geophysical changes.

In Fig. 3.20 the calculated deformation, magnetic and gravity fields are reported for the intrusive source with a width of 1 km (model B).

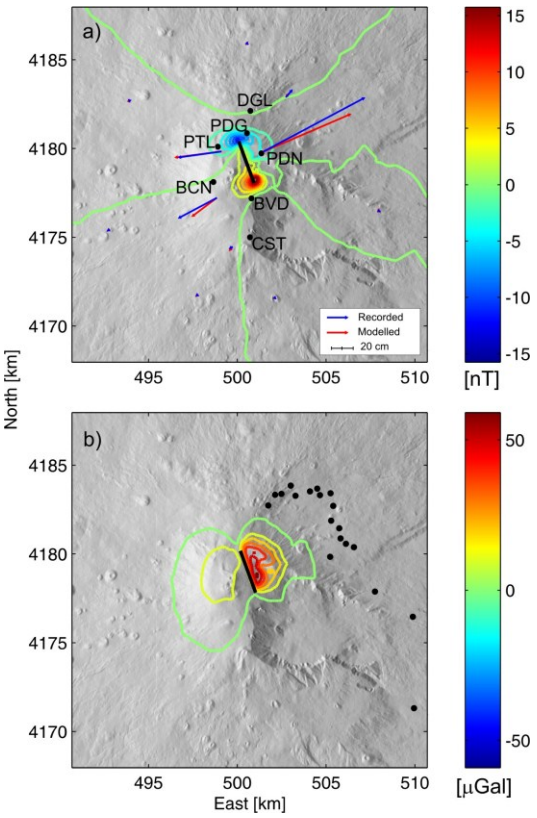

Figure 3.20 – Piezomagnetic changes, ground deformation (a), and gravity changes (b) caused by the magmatic intrusion in model B. Observed (blue arrows) and computed (red arrows) deformation at the permanent GPS stations are also reported. Contour intervals are 2 nT for the piezomagnetic changes (a) and 10 μGal for gravity changes (b).

The match between the observed and the computed magnetic changes is improved at most stations (Fig. 3.17). In particular, the computed piezomagnetic fields at BVD and PDN decrease in amplitude fitting better the magnetic observations. No significant differences are obtained at BCN. Also the ground deformation is slightly changed, even if the fit to the observed deformation is still acceptable (Table 3.3). Indeed, magnetic field seems to be more sensitive to the change in source width.

Although these dislocation models are able to constrain the position and the geometry of the source, a constant-displacement discontinuity, in general, is not the most realistic description of a magma intrusion. An extension fracture is expected to result from magma overpressure on the dike surface and its opening is indeed found as part of the solution (Bonafede and Rivalta, 1999). Therefore, we performed new simulations where the source intrusion was represented by a mode I crack driven by a magmatic overpressure prescribed by constant-pressure boundary conditions (Gudmundson, 2008). We used the source geometry as in the numerical model B. We examine the values of the driving pressure, which fits the observed piezomagnetic changes and ground deformation. A preliminary estimate of the driving pressure ΔP can be given by (Pollard and Segall, 1987):

$$\Delta P = \frac{2E < \Delta u_I >}{\pi W (1-\upsilon)^2} \qquad (3.1)$$

where $<\Delta u_I>$ is the average opening of a 2D crack having a width W embedded in a homogeneous medium with a Young modulus E. This

2D approximation does not account for free surface effects, and for the finite along strike dimension of the dike (Segall et al., 2001). In the crack model the estimate of the pressure change from ground deformation is directly related to the Young modulus. A decrease of the Young modulus requires a decrease of the driving pressure to achieve comparable deformation. On the contrary, when the pressure at the source wall is assigned, the piezomagnetic changes are not affected by variations in the rigidity of the host rocks but only in the initial magnetization (Currenti et al., 2009). Therefore, they can directly provide an estimate about the pressure change, if values of initial magnetization are known. Better resolution of the driving pressure is, therefore, related to the definition and accuracy of the magnetic and elastic medium parameters. Since the former are poorly known, it is advisable to consider values of the medium properties within reasonable ranges. Magnetic properties of volcanic rocks cropping out in the Etna volcano have rarely been measured; however, the few laboratory measurements carried out on recent and historic lava flows show values of remanent magnetization up to 9 A/m (Pozzi, 1977; Tanguy, 1975; Del Negro and Napoli, 2002). The numerical simulations of the piezomagnetic field reveal that, for an initial magnetization ranging between 7 and 9 A/m in the first layer, the related driving pressure varies from 15 to 12 MPa in order to fit the observed magnetic changes (Table 3.3). A lower overpressure would have required unreasonably high values of initial magnetization to obtain comparable piezomagnetic changes. Moreover, the range of overpressure values obtained from piezomagnetic evidence cannot

provide the large observed deformations. Assuming an average magnetization of 8 A/m and a related overpressure of 13 MPa (model C), the match with the magnetic observation is improved (Fig. 3.17), whereas the fit with ground deformation worsens (Table 3.3). Indeed, the dike surface reaches a maximum opening of about 1.4 m, which is lower than the 2 m expected from the dislocation model B. Therefore, a softer medium around the intrusion should be considered to enhance the deformation field. A better match is provided using a Young modulus of 10 GPa (model D), which leads to a maximum opening at the center of the dike of about 2.4 m (Fig. 3.21).

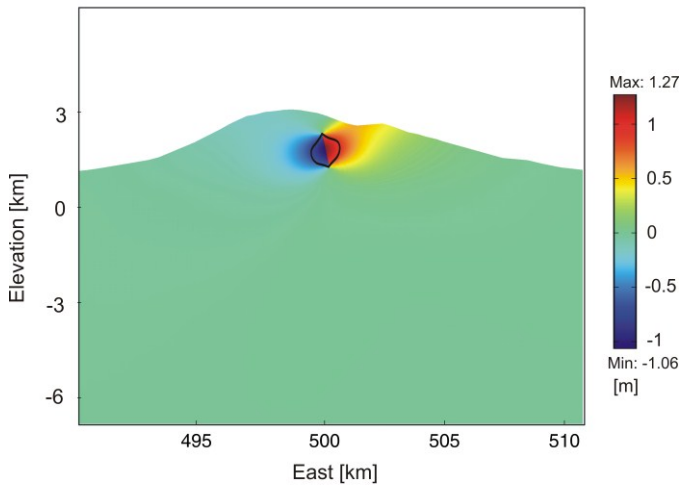

Figure 3.21 – Normal displacement to the dike wall in the numerical model D. The dilation profile (opening exaggerated by a factor 300) for an overpressure of 13 MPa is also reported (black line).

The assumption of a softer medium surrounding the intrusion in model D enhances the deformation with respect to model C, while the overpressure condition within the source provides approximately the same stress, thus maintaining the observed magnetic changes within the range of model C (Table 3.3). The normal displacement along the dike surface is not uniform and shows an oval shape, as expected for a crack model (Fig. 3.21). The opening is greater on the east side of the dike with respect to the west, probably due to the mass deficit in the East sector in correspondence of the Valle del Bove depression.

3.4 Discussions

An integrated modeling of geophysical data is proposed in this chapter. Ground deformation, gravity and magnetic field changes produced by pressure sources and intrusive sources were evaluated by an elastic 3-D model based on Finite Element Method (FEM). The FEM allows for taking into account the real topographic relief and magneto-elastic heterogeneities, appraising their effects on the expected fields.

3-D FEM model was applied to review the 2005-2006 inflation period and the 2008 magma intrusion at Mt Etna and verify the consistency of the joint interpretation of magnetic, gravity and geodetic observations.

For the first case study we assumed the source inverted by Bonforte et al. (2008) using deformation data and obtained that the model is able

to reproduce the principal effects in the pattern of observed magnetic and gravity changes. Since the thermomagnetic effect is the dominant effect and the source is quite deep, the effect of heterogeneity and rough topography don't influence strongly the solution.

Analyzing the second case study, we had to modify the numerical model in order to obtain a better fit with observed data. The intrusive source obtained using the analytical model from magnetic data inversion by Napoli et al. (2008) was firstly used to guide parameter choices for the numerical model. Higher discrepancies between the numerical and analytical solutions are obtained in the intensity of the piezomagnetic field because of the stress concentration near rugged topography. While the topography is known with higher resolution and accuracy, the simple layered model is an over-simplification of the variation of the magneto-elastic parameters in the Etna subsurface. This assumption is due to the poor knowledge of magneto-elastic properties of Etna volcano. Moreover, the solutions could be strongly altered in presence of a more complex heterogeneity as revealed by comparison of different numerical models carried out in Par. 2.4.1.

The source size was modified in the numerical model B to obtain a better match between the observed and the computed geophysical variations at most stations. The numerical solution suggested an intrusive source with a reduced width in agreement with the shallow depth of departure of magma intrusion from the central conduit deduced by Aloisi et al. (2009).

The 2008 intrusion toward the northern flank was arrested in the summit area without downslope propagation and lava emission

occurred only along the E-W eruptive fissure in the upper side of the Valle del Bove. Magma arrest depends strongly on the local stress in the different layers constituting the volcano edifice. The local stress is primarily determined by the loading conditions (tectonic stress, magmatic pressure, or displacement) and the elastic properties of the layers. Local discontinuities characterizing the rift zone may cause the arrest of magma at shallow crustal depths (Maccaferri et al., 2010). It is worth noting that magma intrusion propagates at a shallow depth, where the presence of very fractured and compliant rocks could have favored magma propagation through the medium. Considering that the overpressure of magma with respect to the horizontal stress in the host rock can play a key role for dike opening and propagation (Bonafede and Rivalta, 1999), it is essential to estimate the value or the range of values of driving pressure responsible for the intrusive process. In our numerical model the intrusion process was described in terms of pressure change, and the magma intrusion was modeled as a tensile crack. When the source is assigned in terms of the internal overpressure, the stress changes in the surrounding medium are better constrained than employing a dislocation source. Since the piezomagnetic effect depends directly on the deviatoric stress, it provides direct constraints on the internal overpressure of the intrusion. In this case, the piezomagnetic changes are slightly influenced by the elastic heterogeneity (Currenti et al., 2009) and they are nothing but a kind of stress measurement. Taking advantage of the observed piezomagnetic changes and assuming an initial magnetization of 8 A/m, which is an average reasonable value for

Etnean rocks of the first layer where magma intruded, a driving pressure of 13 MPa and a Young modulus of 10 GPa were estimated (model D). The elastic model seems unable to reproduce the observed deformation, unless lower effective rigidity modulus (60% of the Young modulus assumed for the top layer) is considered. The effective rigidity concept is physically motivated by the hot, highly fractured and deformed shallow rocks surrounding the intrusion. The assumed elastic rheology may not be appropriated in proximity of the source where the medium behavior is better described using anelastic rheologies, such as viscoelastic and elastoplastic (Davis et al., 1974; Currenti et al., 2010; Jellinek et al., 2004). It is reasonable to expect that effectively viscous deformation of wall rocks, heated to well above the normal geotherm in proximity of magmatic sources, will influence the dynamics governing the formation of dikes (Jellinek and DePaolo, 2003; Del Negro et al., 2009). Non-linear rock behavior is consistent with laboratory tests carried out on Etnean rock samples (Rocchi et al., 2004) that revealed an average tensile strength of about 10 MPa and can justify the wide fracture field produced in the northern flank of Etna during the magma propagation. Temporal evolution of magnetic changes, that started simultaneously at all stations and showed a fast decrease in the variations rate just an hour after the beginning of intrusion process (Napoli et al., 2008), highlighted an abrupt decrease of the driving pressure. This was plausibly caused by the simultaneous magma withdrawal from near effusive activity occurring in the Valle del Bove, and it can be considered as the main reason of the magma arrest.

The numerical model D also revealed a non-homogeneous distribution of the displacement produced by intrusion. Particularly, the smallest displacement is observed along the upper west side of the dike where it is well confined by the volcano edifice, while to the east the mass deficit of the Valle del Bove better accommodated the stress field generated by magma intrusion.

On the basis of the results reported in Table 3.3, model D gets better agreement with respect to model C but it is still worse than model B, which seems to provide the best overall fit. However, the integration of laboratory measurements of rock strength and magnetization with the numerical results indicates that better grounded physically models, such as models C and D, are to be explored in the future to improve the data-fit and better constrain the source location and geometry.

The application of 3D FEM model allowed for more accurate interpretations and inferences in modeling-based assessments of geophysical changes associated with volcanic activity.

Chapter 4

FEM and ANN combined approach for predicting pressure sources at Etna volcano

The main goal of volcano modeling is to deduce information about the subsurface distribution of physical properties taking advantage from physical measurements: this represents the *Geophysical Inverse Problem*. Elaborated inverse methods typically combine analytical or numerical forward models with appropriate algorithms to find the best parameter set that minimizes the misfit between the model values and the observations by means of an objective function.

We investigate the ability of a hybrid procedure in which ANNs are used for system identification of forward and inverse geophysical models solved by FEM. The procedure is applied to model the expected geophysical changes at Etna volcano, which constitutes a unique natural laboratory for the understanding of eruptive processes because of the high rate of eruptive events and the high quality geophysical observations gathered by monitoring networks. The 3D numerical model allows to include not only the real topography of Mt Etna but also heterogeneous medium properties inferred from geological evidences and seismic tomography investigations (Chiarabba et al., 2000; Tibaldi and Groppelli, 2002). The ANNs are trained with numerical patterns, obtained computing geophysical changes caused by pressure sources through FEM analysis. We propose an integrated approach in which geophysical data of different nature, that can be ascribed to the same volcanic source, are jointly modeled in order to identify the source parameters with a greater degree of confidence than when only one kind of data is used (Nunnari et al., 2001).

The application of FEM and ANN based modeling is presented to solve both forward and inverse problems. Synthetic patterns are generated by FEM in order to provide a data set large enough to represent the training and testing sets of the possible models within the model space. Firstly, we estimate the volcanic source parameters performing the inversion of ground deformation, magnetic and gravity fields, which are continuously recorded by permanent monitoring

stations at Mt Etna (Bonaccorso and Davis 1999; Bonforte et al., 2008; Del Negro et al., 2004; Napoli et al., 2008; Carbone et al., 2007; 2008). We use the ANN to identify the inverse relation between the geophysical observations and the source parameters. The ANNs, once properly trained, can solve the inversion problem very fast and with an appreciable degree of accuracy. Secondly, we used the ANN to map the forward numerical model with the aim to obtain an immediate approximate solution to be used in any inversion algorithm. This approach retains the computational convenience of forward analytical solutions and is also capable of including the effects of topography and medium heterogeneity. The association of FEM and ANN techniques could be a useful alternative for advancing the model-based assessments of geophysical observations in volcanic areas.

4.1 Forward Problem: FEM solution

Because of the limited amount of volcano-related geophysical changes detected from measurements, we generate synthetic patterns to provide a large number of input/output patterns to train and test the ANN. We compute ground deformation, magnetic and gravity field changes at Mt Etna caused by spherical pressure sources that are quite appropriate for modeling inflation/deflation of magma reservoirs, which are likely to reside at depth greater than 2 km bsl (Corsaro and Pompilio, 2004; Bonforte et al., 2008).

We applied the numerical procedure based on FEM described in chapter 2 to evaluate deformation field changes. The elastostatic problem is solved in a computational domain of a 100x100x50 km using the software PyLith (Aagaard et al., 2008). The horizontal and vertical displacements at the lateral and bottom boundaries of the domain are fixed to zero, representing the vanish displacement at the infinity. The upper boundary is stress free and represents the ground surface. These settings warrant a good accuracy of the numerical solution (Currenti et al., 2008b).

Both irregular topography and medium heterogeneities are included in the FEM model to consider a realistic description of Etna volcanic edifice. The elastic material properties are derived from seismic tomography investigation (Patané et al., 2006).

Pressurization of magmatic sources is also accompanied by gravity and magnetic changes, generally ascribed to the variations of density and magnetization within the magmatic source. The thermo-magnetic effect, caused by thermal demagnetization of magnetic materials, is a mechanism able to produce large magnetic changes. Other magnetic effects, such as piezomagnetism (Sasai, 1991b), are generally not larger than few nanoTeslas (nT). As observed during the last Etna eruptive events (Del Negro and Currenti, 2003; Del Negro et al., 2004; Napoli et al., 2008), detectable piezomagnetic changes are induced by shallow magmatic intrusions within the volcanic edifice (Currenti et al., 2009), whereas negligible piezomagnetic variations are generated by deep pressure sources (> 2 km bsl).

Gravity changes due to a pressure source originate from three different contributions: (i) new mass input from remote distances into the source volume, (ii) relative volume change of the medium arising from compressibility of the surrounding rock, (iii) the displacements of density boundaries (Bonafede and Mazzanti, 1998; Okubo, 1991; Currenti et al., 2007). The last two contributions have a significant effect on the magnitude of the predicted gravity changes when the source resides at shallow depths (Bonafede and Mazzanti, 1998; Charco et al., 2006; Currenti et al., 2007). In case of deep pressure sources these contributions are below microgravity accuracy (Battaglia and Seagall, 2004, Currenti et al., 2007) and are negligible compared to those produced by the input of new mass.

Under these assumptions, we focus on thermomagnetic effect and gravity changes related to mass input, which depend mainly on the magnetization and density contrasts between the source and the surrounding rocks and on the source position. Therefore, they are not affected by the presence of medium heterogeneities. Moreover, for spherical sources the topography effect is due primarily to the distance of the free surface from the magma source rather than the local shape of the free surface. As a result, the thermomagnetic and gravity changes can be computed using the analytical solutions allowing the source depth to vary with topography. The analytical solution of the thermomagnetic change ΔT at the observation point (x, y, z) is expressed as follows (Blakely, 1995):

$$\Delta T = -\frac{\Delta M_m}{4\pi r^3}\left\{1-3\left(\frac{x}{r}\cos I-\frac{z}{r}\sin I\right)^2\right\} \qquad (4.1)$$
$$\Delta M_m = \frac{4}{3}\pi R^3 m$$

where ΔM_m is the magnetic moment, R is the radius of the sphere, m is the magnetization, I is the magnetic inclination, and $r=\sqrt{(x^2+y^2+z^2)}$ where $z=z'+f$ with f the elevation of the observation point above the sea level and z' the source depth with respect to the sea level. The gravity change Δg due to input of mass ΔM_g in a spherical source is expressed as follows (Blakely, 1995):

$$\Delta g = G\Delta M_g \frac{z}{r^3} \qquad (4.2)$$
$$\Delta M_g = \frac{4}{3}\pi R^3 \Delta\rho$$

where $\Delta\rho$ is the density contrast, G is the gravitational constant.

Using the forward models, we generate 1050 synthetic patterns of deformation, magnetic and gravity changes for training and testing the neural network. The procedure of pattern generation is divided in several steps and is executed automatically. Firstly, the computational domain of Mt Etna is meshed into 598948 isoparametric and arbitrarily distorted tetrahedral elements connected by 103424 nodes. The meshed domain, generated with the LaGrit software (http://lagrit.lanl.gov), has a spatial resolution of 300 m in the summit area and around the source location (Fig.4.1).

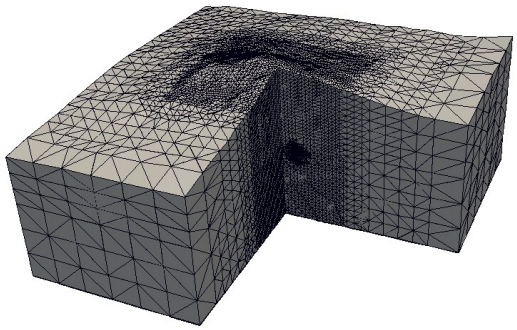

Figure 4.1 - Mesh of the computational domain. The mesh has a spatial resolution of 300 m in the summit area and around the source location and becomes coarser at greater distance.

Then, the parameters of the source are generated with a random distribution in the ranges reported in Table 4.1.

Table 4.1. Ranges of the random generated parameters of the source.

Source Parameters	**Minimum**	**Maximum**
Xc [km]	496	502
Yc [km]	4175	4183
Zc [km]	-9	-1
ΔP [MPa]	50	200
ΔM_m [Am]	$1*10^9$	$4*10^9$
ΔM_g [kg]	$3*10^9$	$150*10^9$

The sources are distributed in a volume that contains all the pressure sources active at Mt Etna during the last decades (Bonforte et. al 2008).

Once all the source parameters are defined, the source volumes are meshed iteratively and introduced in the domain to finally obtain 1050 complete meshes, characterized by the different positions of the source. For each mesh, PyLith was automatically run to solve the elastostatic problem. Given the range of the source depth, the effect of the finite shape of the pressure source can be disregarded (Williams and Wadge, 1998; 2000; Bonafede and Mazzanti, 1998; Tiampo et al., 2000; McTigue, 1987), and the radius R is kept constant to 500 m. As the numerical solutions of the deformation is proportional to the pressure change, all the computations are performed using a constant pressure of 100 MPa and the solutions are then rescaled within the range of the random value of ΔP (Table 4.1). The accuracy of the numerical solution is warranted checking the convergence of the GMRES solver (Aagaard et al., 2008), stopping the iterations when the relative tolerance reaches a threshold of 10^{-9}. By a linear speed-up on a cluster of 20 nodes the computing time reduces from 10 days to 12 hours (Fig. 4.2).

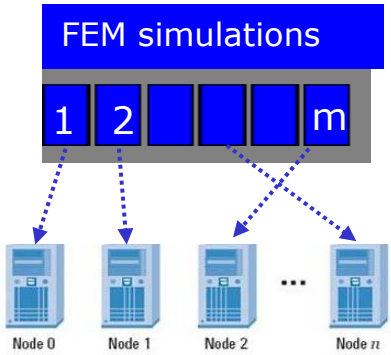

Figure 4.2 - Parallelization of procedure on a cluster of 20 nodes.

In Fig. 4.4 the solution of the vertical displacement is represented on the calculation domain of 100x100x50 km, for one of the sources with random generated parameters in the range reported in Table 4.1.

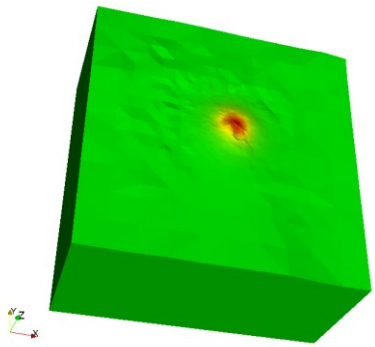

Figure 4.3 - Deformation pattern of the vertical component.

Finally, the solutions are interpolated at the coordinates of the continuously running GPS stations (Fig.4.4).

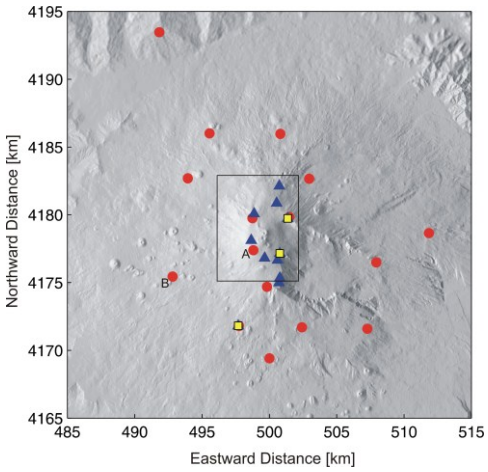

Figure 4.4 - Permanent GPS (red circles), gravity (yellow squares) and magnetic (blue triangles) stations of the monitoring networks on Mt Etna. The black rectangle corresponds to the projection on surface of the volume where the sources are located.

For the same source parameters, magnetic and gravity changes at the locations of the monitoring stations are computed using Eqs (4.1) and (4.2). The gravity and magnetic changes were calculated assuming values of magnetization and density contrast between 4 and 8 A/m (Currenti et al., 2009) and between 100 and 300 kg/m^3 (Corsaro and Pompilio, 2004), respectively.

4.2 Neural Network model

Artificial Neural Networks (ANN) consist in a large number of simple processing elements, called neurons that are connected to each other by means of directed links, each with an associated weight (Haykin, 1999). An activation function controls the amplitude of the neuron's output, adjusting a linear combination of the weighted inputs. ANNs are typically applied for approximating a non linear input-output relationship of the form $\mathbf{y}=f(\mathbf{x})$, where $\mathbf{x}$ and $\mathbf{y}$ are the input and output vectors, respectively. Using the supervised learning scheme (Zurada, 1999; Haykin, 1999), the input-output relationship is determined by looking at the examples of many input-output pairs, which represent the knowledge of the model. In the learning process, the connection weights of the network are changed adaptively to match the actual output of the ANN with the example output. The procedure iterates until the error is small enough.

We apply a class of neural networks called Multilayer Perceptrons (MLPs) to identify both forward and inverse geophysical models. The neural network is trained using many input-output pairs generated solving the forward model. After the training process, the ANN provides a model M that approximates the geophysical model.

In the inverse problem, the model M approximates the function $\boldsymbol{x}=f^{-1}(\boldsymbol{y})$, in the hypothesis that it exists. The ANN inverse model M_i provides an estimate of the source parameters $(\boldsymbol{x})$ as a function of the geophysical observations $(\boldsymbol{y})$. Once the neural network is trained, it is able to approximate the unknown function and to identify, for a set of geophysical observations, the source parameters that better reproduce these variations (Fig.4.5a).

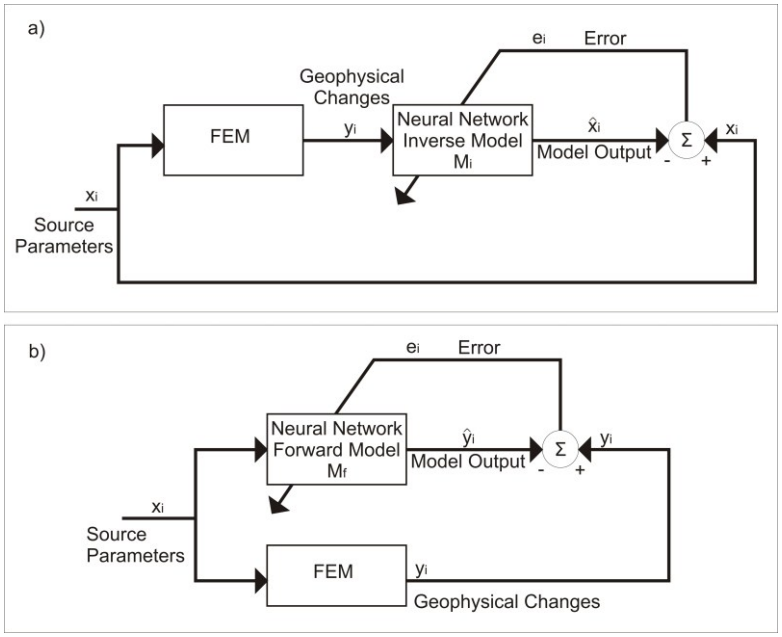

Figure 4.5 - Block diagrams of inverse (a) and forward (b) model identification.

In the forward problem, the model *M* approximates the function $f(\cdot)$ providing an estimate of the geophysical observations ***(y)*** from the assigned source parameters ***(x)***. Closed-form analytical solutions providing the function $f(\cdot)$ are available under the assumption of homogeneous half-space medium, whereas the function $f(\cdot)$ is unknown for complex numerical models, which consider medium heterogeneities and real topography. Therefore, the ANN is trained to identify the forward numerical model M_f using input/output patterns generated from FEM simulations that provide more realistic models. The block diagram of the ANN forward model is reported in Fig. 4.5b.

4.3 Identification results

4.3.1 ANN based inverse model

We firstly implement the ANN inverse model M_i of deformation field, and then we investigate a model M_i able to invert deformation, magnetic and gravity changes together. The MLP neural network is initially trained with a set of 800 input/output patterns, successively the inverse model is tested with a set of 250 patterns that has not been used previously for training. Several network configurations for the deformation inverse model have been tried and the better results are obtained using a three layered network with sigmoidal activation functions. The inputs are the three components of deformation field calculated at 15 stations of the continuously running GPS network and the outputs are the source parameters (position of the source and pressure change). We choose a network with a single hidden layer because we have found experimentally that more than one hidden layer leads to a considerable increase in time required for the learning process without any significant improvement in the accuracy of the solution (Fig. 4.6). Ten hidden neurons are verified to be enough to obtain a compromise between performance and complexity of the network.

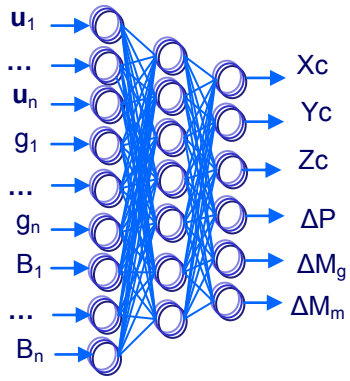

Figure 4.6 - Structure of Artificial Neural Network for inversion of geophysical models.

The accuracy of the inverse model is tested using the Root Mean Square Error (RMSE), whose expression is:

$$RMSE = \sqrt{\frac{1}{N}\sum_{i=1}^{N}(\hat{x}_i - x_i)^2} \qquad (4.3)$$

where $\hat{x}_i$ is the calculated value of the i-th parameter, x_i is the corresponding true parameter, and N is the number of pattern. Since the source parameters have different scales, we also computed the mean percent error $E\%_{abs}$ (Nunnari et al., 2001) to have a normalized measure of the misfit:

$$E\%_{abs} = 100\frac{\sum_{i=1}^{N}|\hat{x}_i - x_i|}{2ND} \qquad (4.4)$$

where D is the range of the parameter. These performance indexes related to the inversion of deformation data are reported in Table 4.2.

Table 4.2. Performance indexes *RMSE* and $E\%_{abs}$ for the inversion of analytical and numerical deformation model and for the integrated numerical model.

Source Parameters	**Deformation (Analytic)**		**Deformation (Numeric)**		**Integrated (Numeric)**	
	RMSE	$E\%_{abs}$	*RMSE*	$E\%_{abs}$	*RMSE*	$E\%_{abs}$
Xc [m]	26.74	0.14	123.17	0.72	154.81	0.89
Yc [m]	31.99	0.11	184.75	0.83	164.18	0.71
Zc [m]	33.46	0.12	153.19	0.72	175.14	0.84
ΔP [MPa]	0.33	0.12	6.84	2.98	5.25	2.61
ΔM_m [Am]	___	___	___	___	$93.3*10^6$	0.82
ΔM_g [kg]	___	___	___	___	$4.94*10^9$	1.04

The ANN is able to approximate with good accuracy the inverse model. For the estimate of the source position the RMSE is less than 200 m and the $E\%_{abs}$ does not reach 1%. A worse accuracy is obtained for the pressure change whose $E\%_{abs}$ is about 3%.

To assess the accuracy of numerical ANN inverse model M_i, we also train and test the network with a set of input-output patterns calculated analytically for an homogenous half-space model. The analytical solutions of the three components of ground deformation field are

computed using the simple and common Mogi source embedded in a homogeneous half-space medium (Mogi, 1958). The components of the displacements ux, uy, uz, computed at the observation point (x,y,z), with the vertical z-axis directing downwards, are the following:

$$u_x = \frac{C}{2\mu}\left\{\frac{x}{r_1^3} + \frac{\lambda+3\mu}{\lambda+\mu}\frac{x}{r_2^3} - \frac{6xz(z+d)}{r_2^5}\right\}$$
$$u_y = \frac{C}{2\mu}\left\{\frac{y}{r_1^3} + \frac{\lambda+3\mu}{\lambda+\mu}\frac{y}{r_2^3} - \frac{6yz(z+d)}{r_2^5}\right\} \qquad (4.5)$$
$$u_z = \frac{C}{2\mu}\left\{\frac{z-d}{r_1^3} - \frac{(\lambda+\mu)z-(\lambda+3\mu)d}{(\lambda+\mu)r_2^3} - \frac{6z(z+d)^2}{r_2^5}\right\}$$

where λ and μ are the Lamé constants, d is the depth of the source, $C = \frac{\Delta P R^3}{2}$, R is the radius of the sphere, ΔP is the pressure change at the source wall, $r_1 = \sqrt{x^2+y^2+(z-d)^2}$, $r_2 = \sqrt{x^2+y^2+(z+d)^2}$.

Better performances are achieved for the analytical inverse model with respect to the numerical one. The $E\%_{abs}$ for all the source parameters is lower than 0.15 %. The main discrepancy between the two models is observed on the pressure change. All source parameters have quite the same value of $E\%_{abs}$ in the analytical inversion, whereas in the numerical inverse model the error on the pressure change is higher with respect to the other parameters. This result could be ascribed to the complex distribution of elastic parameters that affects the deformation of the rock surrounding the source. Under the assumption of elastic rheology, the amplitude of the deformation field

for a spheroidal pressure source is linearly related to the ratio between the pressure and the rigidity modulus ($\Delta P/\mu$). Therefore, it is not straightforward to distinguish whether the perturbation in ground deformation is due to changes in overpressure or in rigidity modulus. The spatial variation of elastic parameters in the 3D numerical model makes the estimate of pressure changes more difficult. However, in the numerical model the error on the estimate of pressure change is still acceptable (Table 4.2). Even if the inverse model to interpolate is more complicated because of the perturbations due to medium heterogeneity and irregular topography, the numerical inversion can be achieved with good accuracy.

We train the neural network with an integrated dataset of ground deformation, magnetic and gravity fields. The neural network used for the integrated inversion is a three layered network, with 59 inputs (the three components of deformation field calculated at 15 stations, thermomagnetic field calculated at 11 stations and gravity filed calculated at 3 stations), 13 hidden neurons, and 6 outputs (position of the source, volume change, magnetic momentum, mass change). In Fig. 4.7 we show the values of the source parameters predicted by the ANN with respect to the output patterns of the testing set, which has not been used for the training.

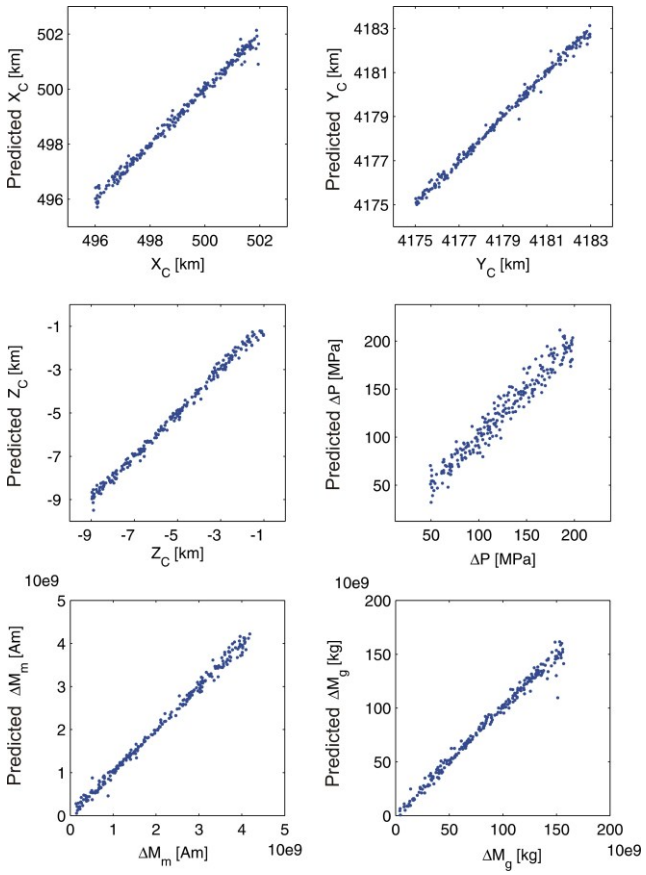

Figure 4.7 - Predicted values of source parameters with respect to output patterns of the testing set for the integrated numerical inversion.

A good match is observed for all source parameters since the real and predicted values lie along the bisector axis with small dispersions (Fig. 4.7). These results demonstrate that the estimated values are well correlated with the ANN predictions. The RMSE and $E\%_{abs}$ for the integrated inversion (Table 4.2) are similar to those obtained inverting

only deformation data. The integrated approach, relying on observations of different kinds, allows to estimate the variations in different geophysical parameters, which independently give insights into the volcano activity. The large number of geodetic measurements usefully supports the inversion of magnetic and gravity observations, coming from a limited number of monitoring stations.

To demonstrate the robustness of the numerical inversion procedure, both for deformation inversion and for integrated inversion, tests were carried out adding white noise to the set of inputs. The value of the noise was calculated as follows (Nunnari et al., 2001):

$$Noise = Xran \frac{\sum_{i=1}^{N} |y_i|}{N} \frac{Perc}{100} \qquad (4.6)$$

where *Xran* is a uniformly distributed random variable in the interval [-1;1], *Perc* is the percentage of noise, y_i is the i-th value of the considered input set (Fig. 4.5a). The ANN trained with noise-free patterns is tested using noise-added patterns to evaluate the robustness of the network for real observed data, which are intrinsically affected by measurement error. We evaluated the $E\%_{abs}$ performance index for different noise levels increasing the *Perc* values from 1 to 10. The mean percent error $E\%_{abs}$ is showed in Fig. 4.6 for numerical inversion of ground deformation, and in Fig. 4.9 for integrated numerical inversion, for both noise-free and noise-added conditions.

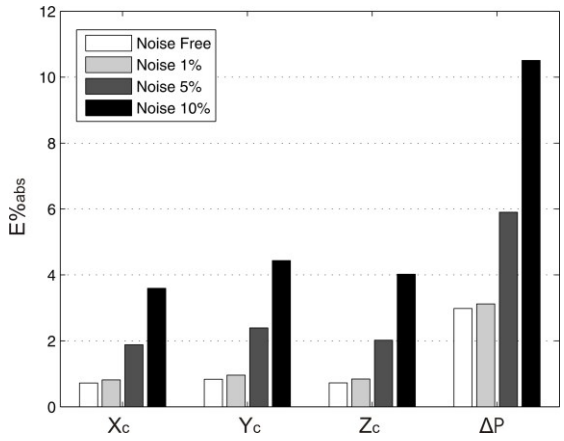

Figure 4.8 - Mean percent error $E\%_{abs}$ for each source parameter using noisy deformation patterns at the inputs of the ANN inverse model.

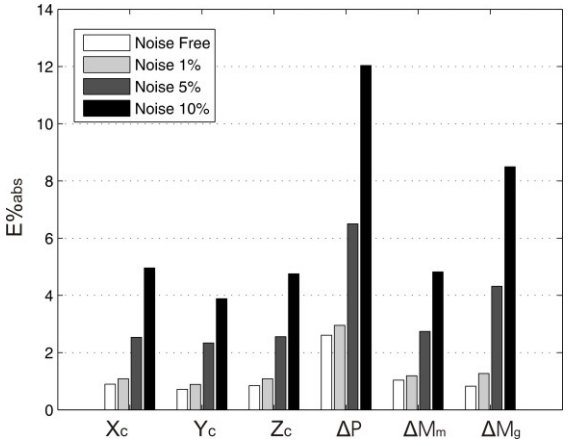

Figure 4.9 - Mean percent error $E\%_{abs}$ for each source parameter using noisy patterns at the inputs of the integrated ANN inverse model.

Although the $E\%_{abs}$ performance index increases with the percentage of noise, it remains smaller than 12% warranting a good accuracy on

the estimate of source parameters also in presence of noise. Moreover it does not appear a significant amplification in the percentage error on source parameters with respect to the percentage of noise introduced in the patterns.

4.3.2 ANN based forward model

The proposed ANN inverse model has the intrinsic limitation to be strictly dependent on both the configuration and the number of measurement stations. If a station does not work and no data are available for one of the input nodes, the learning process has to be performed again using a different neural network structure compliant to the new stations' configuration. To overcome this weakness, a different inversion scheme should be investigated. Instead of identifying the inverse model, the ANN can be trained to provide an approximation of the numerical solutions. Once the network is trained, the numerical solutions of the forward model are immediately available as outputs of the ANN with a computational convenience comparable to the analytical solutions (Fig. 4.5b). The inversion can be performed at a second time also with iterative methods since the solution of the forward model is straightforwardly computed by the ANN, which avoids the computation effort of the full FEM analysis at every iteration step. Moreover, the inverse process is more compliant and flexible to the variation of stations' configuration.

The ANN is trained to identify the forward numerical model M_f only for ground deformation field, since the forward models for the gravity and thermo-magnetic fields are available in closed-form analytical solutions (Eqs. 4.1-4.2). The ANN gives an approximation of the unknown relation between the source parameters and the deformation field in presence of medium heterogeneity and topography (Fig. 4.5b). The neural network is trained to interpolate the function $u_i = F(Xc, Yc, Zc, rx_i, ry_i)$ at each station, where u_i is the deformation at i-th station, *Xc, Yc, Zc* give the position of the source, rx_i, ry_i are the horizontal components of the relative distance between the source and the station. The neural network used for identifying the forward model is a three layered network, with 5 inputs (*Xc, Yc, Zc,* rx_i, ry_i), 20 hidden neurons, 3 outputs (u_x, u_y, u_z). Sigmoidal activation functions were chosen for the first two layers, while a linear activation function was chosen for the output layer.

Using the input/output patterns generated with the FEM, the ANN forward model is trained for each GPS station. The model is validated computing the RMSE for the three deformation components. To provide a reference for the quality of the identification, we rescale the misfit values by the magnitude of the deformation field defining a normalized measure of the error δ_m:

$$\delta_m = \frac{\sum|\hat{u}_m - u_m|}{\sum|u_m|}100\% \qquad (4.7)$$

where u_m is the m-component of the computed deformation using FEM and $\hat{u}_m$ is the deformation estimated by the ANN, with $m = x, y, z$ computed for each deformation component. In Table 4.3, we show the results for two stations, one situated in the summit of volcano and the other at a lower altitude.

Table 4.3. Performance indexes RMSE and normalized misfits δ_m for two stations located near (A in Fig. 4.4) and far (B in Fig. 4.4) from the summit of volcano.

Station		A	B
RMSE [m]	u_x	$6.51*10^{-6}$	$3.70*10^{-6}$
	u_y	$7.72*10^{-6}$	$2.50*10^{-6}$
	u_z	$9.12*10^{-6}$	$2.30*10^{-6}$
Normalized misfit δ_m [%]	u_x	11.9	6.03
	u_y	10.9	7.75
	u_z	6.90	5.03

The results demonstrate that the neural network is able to identify with a good accuracy the forward numerical model of deformation field despite the complexity introduced by the medium heterogeneity and topography. It is worth noting that the error at the station located out from the summit is smaller than that obtained for the summit station, where numerical solution is strongly influenced by topography and heterogeneity (Fig.4.4). This result highlights the significant effect that these parameters have on the solution.

4.4 Discussions

A combined approach is proposed using neural networks and numerical models for the estimation of pressure source parameters in volcanic regions. ANN is trained to identify the unknown model using patterns obtained by numerical FEM solutions. This method permits to interpret geophysical data avoiding the intrinsic limitation of analytical solutions and providing a more realistic description of volcanic processes. Both ANN and FEM have demonstrated to be appropriate for representing geophysical models at Mt Etna, taking the ability of ANN to learn complex non-linear behavior and that of FEM to include 3D realistic features in models.

Firstly, ANN is used in inverse scheme to identify the source parameters from geophysical observations. The results show that, notwithstanding the high nonlinearity of the considered inverse problems, it can be solved with satisfactory accuracy both for ground deformation inversion and for the integrated inversion of ground deformation, magnetic and gravity changes. Moreover, the inverse model provides an acceptable estimate of source parameters even in presence of noise, which intrinsically affects the geophysical measurements.

Secondly, neural approach is used to map the forward numerical model, reducing the high computational time usually necessary to run the FEM model in iterative inversion schemes. This approach permits to have a straightforward solution of numerical model that can substitute the analytical solution in any inversion technique, providing a more realistic description of geophysical changes in volcanic area by taking into account the real topography and medium heterogeneities.

Results show that the neural network/finite element modeling can be efficiently used in the identification of both forward and inverse numerical models. This approach allows for an accurate estimation of source parameters in a realistic description of volcanic areas, which is of great significance for both the correct interpretation of geophysical data and for the assessment of volcanic hazard.

Conclusions

This thesis represents a discussion on the issues relative to numerical modeling in volcano geophysics yielding advances in the procedures for forward and inverse modeling of monitoring data and volcano phenomena.

Firstly, numerical forward models were implemented in order to overcome the intrinsic limitation provided by the half-space assumption and provide more realistic models which consider topographic effects as well as complicated distribution of medium properties. In particular, the FEM approach presented here allows considering a picture of a fully 3-D model of Etna volcano to evaluate deformation, magnetic and gravity changes caused by overpressure and dyke source in a 3-D formulation.

Secondly, a numerical geophysical inverse problem was outlined and solved. A hybrid approach for forward and inverse geophysical modeling, based on Artificial Neural Networks (ANN) and Finite Element Method (FEM), is proposed in order to properly identify the parameters of volcanic pressure sources from geophysical observations at ground surface. ANNs are used to interpolate the complex non linear relation between geophysical observations and source parameters both for forward and inverse modeling.

We applied the numerical model and the hybrid ANN-FEM approach at Etna volcano, which offer exemplary case studies to validate the capability of the proposed integrated approach for imaging the pressurization and intrusive processes occurring in the volcano. The results show that the proposed approach is a powerful tool for a straightforward and accurate estimation of source parameters in volcanic regions.

Comparisons are made between analytical and numerical solutions of forward models in order to estimate the differences that could be caused by medium heterogeneities and topography on piezomagnetic field. Our results highlight that when topography and magneto-elastic heterogeneities are included in the numerical models, the piezomagnetic field changes show significant deviations from the homogeneous half-space solution. The numerical models of the piezomagnetic field showed significant differences in presence of strong magnetization contrasts and in proximity of steep cliffs, that is, at the volcano summit.

Then, the numerical approach was applied to review the 2005-2006 inflation period and the 2008 magma intrusion detected at Mt Etna by geophysical data. Our results show that the numerical model is able to reproduce the geophysical observations. A better knowledge of density and magnetization distribution inside the volcanic edifice is essential for improvement of integrated numerical models that may discriminate the main factors influencing the energetic levels involved in the opening and propagation of dikes.

Since geodetic and gravity data provide information on the strain field, while piezomagnetic changes give constraints on the stress field, the integrated modeling gives insights on Mt Etna rheology and dike overpressure involved in the magma propagation and improves understanding of dike emplacement in the northern sector of the volcano. This information could provide a better knowledge of the dike intrusion processes and the rheological properties of rocks in the near field of emplaced dikes. That contributes to a more accurate evaluation of the hazard associated with the onset of Etna lateral eruptions, which are usually supplied by magma through fractures opened by magmatic overpressure.

Our FEM-based approach improves the reliability of model-based inference of source parameters obtained during monitoring of Etna activity, that can prelude to an impending eruption.

Although the 3D FEM models and the hybrid FEM-ANN approach were tested and validated at Mt Etna, the developed procedure are so flexible that can be applied to other volcanoes to improve the reliability of modeling-based assessment of geophysical signals and, hence, to advance the understanding of volcanic processes.

Bibliography

AAGAARD, B., S. KIENTZ, M. KNEPLEY, L. STRAND, & C. WILLIAMS (2008): PyLith User Manual, Version 1.3, Computational Infrastructure for Geodynamics. URL:www.geodynamics.org/cig/software/short/pylith/pylith_book-1.3.pdf

ADLER, P., J. L. LE MOUËL AND J. ZLOTNICKI, (1999): Electrokinetic and Magnetic Fields Generated by Flow through a Fracture Zone: A Sensitivity Study for La Fournaise Volcano, *Geophys. Res.Lett.,* 26, 795.

AGIP S.p.A., 1977. Temperature sotterranee. Grafiche Fili Brugora, Milano, p. 1390.

AJMERA T., RASTOGI A.K. (2008): Artificial Neural Network Application on Estimation of Aquifer Transmissivity, *Journal of Spatial Hydrology*, Vol.8, No.2, 15-31.

ALOISI, M., BONACCORSO, A., CANNAVO`, F., GAMBINO, S., MATTIA, M., PUGLISI G., BOSCHI, E. (2009): A new dyke intrusion style for the Mount Etna May 2008 eruption modelled through continuous tilt and GPS data. *Terra Nova*, 00, 1–6.

ARENA P., FORTUNA L., MUSCATO G., XIBILIA M. G. (1998): Neural Networks in Multidimensional Domains: fundamentals and new trends in modelling and control, *Lecture Notes in Control and Information*, Springer, vol. 234.

BATTAGLIA M., SEGALL P., MURRAY J., CERVELLI P. & LANGBEIN J., (2003): The mechanics of unrest at Long Valley caldera, California: 1. Modeling the geometry of the source using GPS, leveling and two-color EDM data, *J. Volcan. Geotherm. Res.,* 127, 195-217.

BATTAGLIA, M., & SEGALL, P., (2004): The Interpretation of gravity changes and crustal deformation in active volcanic areas, *Pure Appl. Geophys.,* 161, 1453 - 1467.

BLAKELY, R. J. (1995): *Potential Theory in Gravity and Magnetic Applications*, Cambridge University Press, New York.

BONACCORSO A. AND DAVIS P.(1999): Models of ground deformation from vertical volcanic conduits with application to eruptions of Mount. St. Helens and Mount Etna, *J. Geophys.Res.*, 104, 10531-10542, 1999.

BONACCORSO, A., and DAVIS, P. M., (2004): Modeling of ground deformation associated with recent lateral eruptions: Mechanics of magma ascent and intermediate storage at Mount Etna, in Mount Etna: Volcano Laboratory, *Geophys. Monogr. Ser.,* vol. 143, edited by S. Calvari et al., pp. 293– 306, AGU, Washington.

BONACCORSO A., CALVARI S., COLTELLI M., DEL NEGRO C. & FALSAPERLA S., (2004): Mt. Etna: Volcano Laboratory. American Geophysical Union, *Geophysical Monograph,* 143, pp. 369.

BONACCORSO, A., CIANETTI, S., GIUNCHI, C., TRASATTI, E., BONAFEDE, M. and BOSCHI E. (2005): Analytical and 3D numerical modeling of Mt. Etna (Italy) volcano inflation. *Geophys. J. Int.,* 163, 852-862.

BONACCORSO A., BONFORTE A., CURRENTI G., DEL NEGRO C., DI STEFANO A., GRECO F. (2011): Magma storage, eruptive activity and flank instability: Inferences from ground deformation and gravity changes during the 1993–2000

recharging of Mt. Etna volcano, *J. Volcanol. Geotherm. Res.*, doi:10.1016/j.jvolgeores.2011.01.001.

BONAFEDE M., MAZZANTI M. (1998): Modelling gravity variations consistent with ground deformation in the Campi Flegrei caldera (Italy), *J. Volcanol. Geotherm. Res.* 81, 137-157.

BONAFEDE, M., RIVALTA, E. (1999): On tensile cracks close to and across the interface between two welded elastic half-spaces, *Geophys. J. Int.*138, 410-434.

BONFORTE A., BONACCORSO A., GUGLIELMINO F., PALANO M., PUGLISI G. (2008): Feeding system and magma storage beneath Mt. Etna as revealed by recent infation/deflation cycles, *Journal Geophys. Res.*, 113, B05406, doi:10.1029/2007JB005334.

BRANCA, S., COLTELLI, M., DE BENI, E. and WIJBRANS, J., (2007): Geological evolution of Mount Etna volcano (Italy) from earliest products until the first central volcanism (between 500 and 100 ka ago) inferred from geochronological and stratigraphic data*, Int. J. Earth. Sci.* DOI 10.1007/s00531-006-0152-0

BUDETTA, G., CARBONE, D., GRECO, F. and RYMER, H. (2004): Microgravity studies at Mount Etna (Italy), in Mount Etna: Volcano Laboratory, *Geophys. Monogr. Ser.,* vol. 143, edited by S. Calvari et al., pp. 221– 240, AGU, Washington, D.C.

BUDETTA, G., ET AL. (2008), Osservazioni gravimetriche e magnetiche. Aggiornamento dello stato di attivita` dell'Etna:15 maggio 2008, *INGV Rep. UFGM2008/05,* Ist. Naz. di Geofis. e Vulcanol., Rome.

BURTON M.R., M. NERI, D. ANDRONICO, S. BRANCA, T. CALTABIANO, S. CALVARI, R. A. CORSARO, P. DEL CARLO, G. LANZAFAME, L. LODATO, L. MIRAGLIA, G. SALERNO, L. SPAMPINATO (2005): Etna 2004-2005: An

archetype for geodynamically-controlled effusive eruptions, *Geophysical Research Letters*, 32, 9, doi:10.1029/ 2005GL022527.

CAI Y. & WANG C.Y. (2005): Fast finite-element calculation of gravity anomaly in complex geological regions, *Geophys. J. Int.,* 162, 696-708

CARBONE D., CURRENTI G. & DEL NEGRO C., (2006): Elastic model for the gravity and elevation changes prior to the 2001 eruption of Etna volcano, *Bull. Volcanol.*.

CARBONE D., CURRENTI G., DEL NEGRO C. (2007): Elastic model for the gravity and elevation changes prior to the 2001 eruption of Etna volcano, *Bull. Volcanol.,* 69, 553-562, DOI 10.1007/s00445-006-0090-5.

CARBONE, D., CURRENTI, G., DEL NEGRO, C.(2008): Multi-objective genetic algorithm inversion of ground deformation and gravity changes spanning the 1981 eruption of Etna volcano. *J. Geophys. Res.,* 113, B07406, doi:10.1029/2006JB004917.

CAYOL, V. and CORNET, F.H. (1998): Effects of topography on the interpretation of the deformation field of prominent volcanoes-Application to Etna, *Geophys. Res. Lett.,* 25(11), 11,979–11,982.

CHAMEKH, A.; BEL HADJ SALAH, H.; HAMBLI, R. (2009): Inverse technique identification of material parameters using finite element and neural network computation, *The International Journal of Advanced Manufacturing Technology*, Volume 44, Numbers 1-2, pp. 173-179(7).

CHARCO, M., FERNANDEZ, J., TIAMPO, K., BATTAGLIA, M., KELLOGG, L., MCCLAIN, J. & RUNDLE, J. B., (2004): Study of volcanic sources at Long Valley Caldera, California, using gravity data and a Genetic Algorithm inversion technique,

Pure Appl. Geophys., 161, 1399–1413. doi:10.1007/s00024-004-2511-8.

CHARCO, M., J. FERNÁNDEZ, F. LUZÓN, AND J. B. RUNDLE (2006): On the relative importance of self-gravitation and elasticity in modeling volcanic ground deformation and gravity changes, *J. Geophys. Res.*, 111, B03404, doi:10.1029/2005JB003754.

CHIARABBA, C., AMATO, A., BOSCHI, E. and BARBERI, F., (2000): Recent seismicity and tomographic modeling of the Mount Etna plumbing system, *J. Geoph. Res.,* 105(B5), 10,923–10,938.

COMSOL MULTIPHYSICS 3.4, 2008. Comsol AB, Stockholm, Sweden.

CORSARO, R. and POMPILIO, M. (2004): Buoyancy-controlled eruption of magmas at Mt Etna, *TerraNova,* 16, 16–22.

CURRENTI G., DEL NEGRO C., NUNNARI G. (2005):Inverse modelling of volcanomagnetic fields using a genetic algorithm technique. *Geophys J Int* 163, 403–418. doi: 10.1111/j.1365-246X.2005.02730.x.

CURRENTI G., DEL NEGRO C., GANCI G.(2007): Modelling of ground deformation and gravity fields using finite element method: an application to Etna volcano. *Geophys. J. Int.* 169, 775–786. doi: 10.1111/j.1365-246X.2007.03380.x.

CURRENTI, G., DEL NEGRO, C., GANCI, and G., SCANDURA, D. (2008a): 3D numerical deformation model of the intrusive event forerunning the 2001 Etna eruption. *Phys. Earth Planet. Interiors,* doi:10.1016/j.pepi.2008.05.004.

CURRENTI, G., DEL NEGRO, C., GANCI, G., and WILLIAMS, C., (2008b): Static stress changes induced by the magmatic intrusions during the 2002-2003 Etna eruption, *J. Geophys. Res.*, 113, B10206, doi:10.1029/2007JB005301.

CURRENTI, G., DEL NEGRO, C., SASAI, Y. (2008c): Time dependent piezomagnetic fields in viscoelastic medium, *Geophys. J. Int.,* 172, 536–548.

CURRENTI G., DEL NEGRO C., DI STEFANO A., NAPOLI R. (2009): Numerical simulation of stress induced piezomagnetic fields at Etna volcano, *Geophys. J. Int.* 179, 1469–1476 doi: 10.1111/j.1365-246X.2009.04381.x.

CURRENTI, G., BONACCORSO, A., DEL NEGRO, C. AND SCANDURA, D. (2010): Elasto-plastic modeling of volcano ground deformation, with application on Mt Etna, *Earth Planet. Sci. Lett.,* 296, 311-318, doi:10.1016/j.epsl.2010.05.013

CURRENTI G., NAPOLI R., DI STEFANO A ., GRECO F., DEL NEGRO C. (2011): A 3D integrated geophysical modeling for the 2008 magma intrusion at Etna: constraints on rheology and dike overpressure, *Physics of the Earth and Planetary Interiors* 185, 44–52, doi:10.1016/j.pepi.2011.01.002.

DAVIS, P.M., HASTIE, L.M., STACEY, F.D., (1974): Stresses within an active volcano – with particular reference to Kilauea. *Tectonophysics* 22, 355–362.

DAVIS, P. M. (1976): The computed piezomagnetic anomaly field for Kilauea volcano, Hawaii, *J. Geomag. Geoelectr*., 28, 113-122.

DAVIS P.M., (1986): Surface deformation due to inflation of an arbitrarily oriented triaxial ellipsoidal cavity in an elastic half-space, with reference to Kilauea volcano, Hawaii, *J. Geophys. Res.,* 91, 7429–7438.

DE GORI, P., CHIARABBA, C. and PATANE`, D. (2005): Qp structure of Mount Etna: Constraints for the physics of the plumbing system, *J. Geophys. Res.,* 110, B05303, doi:10.1029/2003JB002875.

DEL NEGRO, C. and FERRUCCI, F. (1998): Magnetic history of a dyke on Mount Etna (Sicily) *Geophys. J. I.,*133, 2, 451-458.

DEL NEGRO, C. and NAPOLI, R. (2002): Ground and marine magnetic surveys of the lower eastern flank of Etna volcano (Italy) *Journal of Volcanology and Geothermal Research,* 114, 357-372.

DEL NEGRO C., NAPOLI R. and SICALI A. (2002): Automated system for magnetic monitoring of active volcanoes, *Bull. Volcanol.,* 64 94– 99.

DEL NEGRO, C. and CURRENTI, G. (2003): Volcanomagnetic signals associated with the 2001 flank eruption of Mt. Etna (Italy), *Geophys. Res. Lett.,* 30, 7, 1357, doi:10.1029/2002GL015481.

DEL NEGRO, C., CURRENTI, G., NAPOLI, R. and VICARI, A., (2004): Volcanomagnetic changes accompanying the onset of the 2002–2003. Eruption of Mt. Etna (Italy), *Earth Planet. Sci. Lett.*, 229, 1–14.

DEL NEGRO, C., G. CURRENTI, AND D. SCANDURA (2009): Temperature-dependent viscoelastic modeling of ground deformation: application to Etna volcano during the 1993-1997 inflation period. *Phys. Earth Planet. In.,* 172, 3-4, 299-309.

DI GRAZIA, G., CANNATA, A., MONTALTO, P., PATANE`, D., PRIVITERA, E., ZUCCARELLO, L., BOSCHI, E. (2009): A multiparameter approach to volcano monitoring based on 4D analyses of seismo-volcanic and acoustic signals: The 2008 Mt. Etna eruption, *Geophys. Res. Lett,* 36, L18307, doi:10.1029/2009GL039567.

DI STEFANO A., CURRENTI G., DEL NEGRO C., FORTUNA L., NUNNARI G. (2010): FEM and ANN combined approach for predicting pressure source parameters at Etna volcano, *Nonlin. Processes Geophys.,* 17, 1–10.

GUDMUNDSSON, A., FRIESE, N., GALINDO, I., PHILIPP, S. L. (2008): Dike-induced reverse faulting in a graben, *Geology*, 2008, 36, 123-126, doi: 10.1130/G24185A.1.

HACIB T., MEKIDECHE M.R., FERKHA N. 82007): MPL Neural Network and FEM for the Inverse Problem of parameters Identifications, *International Journal of Electrical and power Engineering 1* (2), 231-238.

HAGIWARA Y.(1977): The Mogi model as a possible cause of the crustal uplift in the eastern part of Izu Peninsula and related gravity change, *Bull. Earthq. Res. Inst.,* Univ. Tokyo, 52, 301–309.

HAYKIN S. (1999): *Neural Networks: A comprehensive foundation,* Englewood Cliffs, NJ:Prentice-Hall, New York.

HILDENBRAND, T.G., ROSENBAUM, J.G. and KAUAHIKAUA, J.P. (1993): Aeromagnetic study of the Island of Hawaii, *J. Geophys. Res.*, 98, 4099-4119.

JELLINEK, A.M. AND D.J DEPAOLO (2003): A model for the origin of large silicic magma chambers: Precursors of catastrophic caldera-forming eruptions, *Bull. Volcanol.* 65, 363-381.

JELLINEK, A.M., M. MANGA, M.O. SAAR (2004): Did melting glaciers cause volcanic eruptions in eastern California? Probing the mechanics of dike formation, *J. Geophys. Res.,* 109, B9, B09206, doi: 10.1029/2004JB002978.

JOUSSET P., MORI H. & OKADA H, (2003): Elastic models for the magma intrusion associated with the 2000 eruption of Usu Volcano, Hokkaido, Japan, *J. Volcan. Geotherm. Res.,* 2607,1-26.

KEAREY, P. and BROOKS, M. (1991): An introduction to geophysical exploration. Second edition. *Blackwell Scientific Publications,* Oxford, pp. 254.

LANGER H., NUNNARI G, OCCHIPINTI L. (1996): Estimation of seismic waveform governing parameters with neural networks, *Journal of Geophysical Research,* Vol. 101, NO.B9, pp 20,109-20,118.

LUNGARINI L., TROISE, C., MEO, M. and DE NATALE, G. (2005): Finite element modelling of topographic effects on elastic ground deformation at Mt. Etna, *J. Volcan. Geotherm. Res.*, 144, 257-271.

MACCAFERRI, F., BONAFEDE, M. AND RIVALTA, E., (2010): A numerical model of dyke propagation in layered elastic media, *Geophys. J. Int.* 180, 1107–1123, doi: 10.1111/j.1365-246X.2009.04495.x

MAUGERI S.R., NUNNARI G., OCCHIPINTI L., PUGLISI G. (1996): A neural approach for the inversion of a dislocation model, *Cahiers du Centre Europeen de Geodynamique et the Seismologie*, Vol 12, pp 141-149.

MAUGERI S.R., NUNNARI G., PUGLISI G.(1997): Inverting ground deformation data: a comparison between the least squares method and the neural approach, *Acta Vulcanologica* Vol.9 (½) , pp 135-140.

MCTIGUE D. F. (1987): Elastic Stress and Deformation Near a Finite Spherical Magma Body: Resolution of the Point Source Paradox, *Journal of Geophysical Research,* Vol 92, no. B12, pp. 12931-12940.

MOGI, K. (1958): Relations between the eruptions of various volcanos and the deformations of the ground surfaces around them, *Bull. Earthq. Res. Inst.,* Univ. Tokyo, 36, 99–134.

MULIANA A., STEWARD R., HAJ-ALI R., SAXENA A. (2002): Artificial Neural Network and Finite Element Modeling of Nanoindentation Tests, *Metallurgical and Materials Transactions* A, Vol. 33A, 139-1947.

MURAKAMI H., (1989): Geomagnetic fields produced by electrokinetic sources, *J. Geomagn. Geoelectr.,* 41, 221–247.

MURASE M., IRWAN M., KARIYA S., TABEI T., OKUDA T., MIYAJIMA, R., OIKAWA, J., WATANABE, H., KATO, T., NAKAO, S., UKAWA, M, FUJITA, E., OKAYAMA, M.,

KIMATA, F. & FUJII, N., (2006): Time dependent model of magma intrusion in and around Miyake and Kozu Islands, Central Japan in June–August, 2000, *Volcanol. Geotherm. Res.,* 150, 213– 231.

NAGATA, T. (1970): Basic magnetic properties of rocks under mechanical stresses, *Tectonophysics,* 9, 167-195.

NAPOLI R., CURRENTI G., DEL NEGRO C., GRECO F., SCANDURA D., (2008): Volcanomagnetic evidence of the magmatic intrusion on 13th May 2008 Etna eruption, *Geophys. Res. Lett.*,35, L22301, doi:10.1029/2008GL035350.

NAPOLI R., CURRENTI G, DEL NEGRO C., DI STEFANO A., GRECO F., BOSCHI E. (2011): Magnetic features of the magmatic intrusion occurred in 2007 eruption at Stromboli Island (Italy.) *Bullettin of Volcanology,* DOI 10.1007/s00445-011-0473-0.

NERI, M. AND V. ACOCELLA (2006): The 2004-05 Etna eruption: implications for flank deformation and structural behavior of the volcano. *J. Volcanol. Geotherm. Res.,* 158, 195-206, DOI:10.1016/j.jvolgeores.2006.04.022.

NUNNARI G., BERTUCCO L., FERRUCCI F. (2001): A Neural Approach to the Integrated Inversion of Geophisical Data Types, IEEE Transaction on Geosciences and Remote Sensing, 39, 4, 736-748.

NUNNARI G., PUGLISI G., GUGLIELMINO F. (2005): Inversion of SAR data in active volcanic areas by optimization techniques, *Nonlin. Processes Geophys.,* 12, 863-870.

OKADA Y., (1985): Surface deformation due to shear and tensile faults in a half-space. *Bull. Seism. Soc. Am*. 75, 1135-1154.

OKADA, Y. (1992): Internal deformation due to shear and tensile faults in a half-space. *Bull. Seism. Soc. Am.* 82, 1018-1040.

OKUBO, S. & H. WATANABE, (1989). Gravity change caused by a fissure eruption, *Geophys. Res. Lett.,* 16, 445–448.

OKUBO S. (1991): Potential and gravity changes raised by point dislocations, *Geophys. J. Int.* 105, 573-586.

OKUBO S. (1992): Gravity and Potential Changes due to Shear and Tensile Faults in a Half-Space, *J. Geophys. Res.,* 97(B5), 7137-7144.

OKUBO, A. and OSHIMAN, N. (2004): Piezomagnetic field associated with a numerical solution of the Mogi model in a non-uniform elastic medium. *Geophys. J. Int.,* 159, 509-520.

OSHIMAN, N. (1990): Enhancement of tectonomagnetic change due to non-uniform magnetization in the Earth's crust – Two-Dimensional case studies. *J. Geomag. Geoelect.,* 42, 607-619.

PATANÈ, D., BARBERI, G., COCINA, O., DE GORI, P. and CHIARABBA, C. (2006): Time-Resolved Seismic Tomography Detects Magma Intrusions at Mount Etna. *Science*, 313, 821-823.

POLLARD, D.D., AND P. SEGALL (1987): Theoretical displacements and stresses near fractures in rock: with application to faults, joints, veins, dikes, and solution surfaces, *In Fracture Mechanics of Rock*, Academic Press, p. 227-349.

POZZI, J.P. (1977): Effects of stresses on magnetic properties of volcanic rocks, *Phys. Earth Planet. Inter.,* 14, 77-85.

PREDA G., CRANGANU-CRETU B., HANTILA F., MIHALACHE O., CHEN Z., MIYA K. (2002): Nonlinear FEM–BEM Formulation and Model-Free Inversion Procedure for Reconstruction of Cracks Using Pulse Eddy Currents, *IEEE Transaction on Magnetics,* Vol. 38, No. 2.

ROLPH, T.C. (1992): High field intensity results from recent and historic lavas, *Phys. Earth Planet. Inter.,* 70, 224-230.

ROCCHI, V., SAMMONDS, P.R., KILBURN, C.R.J. (2004): Fracturing of Etnean and Vesuvian rocks at high temperatures and low pressures, *J. Volc. Geother. Res.* 132, 137-157

ROSENBAUM, J.G. (1993): Magnetic grain-size variations through an ash flow sheet: Influence on magnetic properties and implications for cooling history. *J. of Geoph. Res.,* 98, 11,715-11,727.

RYMER, H., (1994): Microgravity changes as a precursor to volcanic activity, *J. Volcanol. Geotherm. Res.,* 61, 311-328.

RYMER H., FERRUCCI F. and LOCKE C. A.(1998): Mount Etna: monitoring in the past, present and future, *Geological Society,* London, Special Publications; 143; 335-347 doi:10.1144/GSL.SP.1998.143.01.22

SAKANAKA, S., OSHIMAN, N. and SUMITOMO, N. (1997): A Hybrid calculation method of tectonomagnetic effect using BEM and the surface integral representation of the piezomagnetic potential – Two dimensional case study. *J. Geomag. Geoelect.*, 49, 101-118.

SALTAN M., SEZGIN H. (2007): Hybrid neural network and finite element modeling of sub-base layer material properties in flexible pavements, *Materials and Design* 28, 1725–1730.

SASAI, Y. (1986): A Green's function for tectonomagnetic problems in an elastic half-space, *J. Geomag. Geoelectr.,* 38, 949-969.

SASAI, Y., (1991a): Piezomagnetic field associated with the Mogi model revisited: analytic solution for finite spherical source, *J. Geomag. Geoelectr.,* 43, 21-64.

SASAI, Y. (1991b). Tectonomagnetic modeling on the basis of the linear piezomagnetic effect, *Bull. Earthq. Res. Inst.*, Univ. Tokyo, 65, 585-722.

SCHIAVONE, D. AND M. LODDO (2007): 3-D density model of Mt. Etna Volcano (Southern Italy), *J. Volcanol. Geoth. Res*. 164, 161–175.

SEGALL, P., CERVELLI, P., OWEN, S., LISOWSKI, M., MIKLIUS, A., (2001): Constraints on Dike Propagation from

Continuous GPS Measurements, *Geophys. Res.,* 106, 19,301-19,318.

STACEY, D. and BANERJEE, S.K. (1974): The physical principles of rock magnetism, *Dev. Solid Earth Geophys.,* 5,pp.117, Elsevier Scientific, Amsterdam.

SZIDAROVSZKY F., COPPOLA E., LONG J., HALL A., POULTO M. (2007): A Hybrid Artificial Neural Network-Numerical Model for Ground Water Problems, *Ground Water,* Vol. 45, No. 5, 590-600.

TANGUY, J.C. (1975): Intensity of the geomagnetic field from recent Italian lavas using a new palaeointensity method, *Earth Plan. Sci. Lett.,* 27, 314-320.

TAUXE, L., DEINO, A.D., BEHRENSMEYER, A.K. and POTTS, R. (1992): Pinning down the Brunhes/Matuyama and upper Jaramillo boundaries: As reconciliation of orbital and isotopic time scales. *Earth Planet. Sci. Lett.,* 109, 561-572.

TIAMPO, K.F., RUNDLE, J.B., FERNANDEZ, J., LANGBEIN, J.O. (2000): Spherical and ellipsoidal volcanic sources at Long Valley caldera, California, using a genetic algorithm inversion technique. *J. Volcan. Geotherm. Res.,* 102, 189-206.

TIBALDI, A. and GROPPELLI, G. (2002): Volcano-tectonic activity along structures of the unstable ne flank of Mt. Etna (italy) and their possible origin. *J. Volcan. Geotherm. Res.,* 115, 277-302.

TRASATTI E., GIUNCHI C. AND PIANA AGOSTINETTI N. (2008): Numerical inversion of deformation caused by pressure sources: application to Mount Etna (Italy) *Geophys. J. Int*. 172, 873–884, doi: 10.1111/j.1365-246X.2007.03677.x.

TRIC, E., VALET, J.P., GILLOT, P.Y. and LEMEUR, I. (1994): Absolute paleointensities between 60 and 160 kyear BP from Mount Etna (Sicily). *Phys. Earth Planet. Inter.,* 85, 113-129.

UMBRELLO D., AMBROGIO G., FILICE L., SHIVPURI R.(2008): A hybrid finite element method–artificial neural network

approach for predicting residual stresses and the optimal cutting conditions during hard turning of AISI 52100 bearing steel, *Materials and Design* 29, 873–883.

UTSUGI, M., NISHIDA, Y. and SASAI, Y. (2000): Piezomagnetic potentials due to an inclined rectangular fault in a semi-infinite medium, *Geophys. J. Int.,* 140, 479-492.

VOIGHT B., HOBLITT R., CLARKE A., LOCKHART A., MILLER A., LYNCH L. & MCMAHON J., (1998): Remarkable cyclic ground defomation monitored in real-time on Montserrat, and its use in eruption forcastin, *Geophys. Res. Lett.,* 24, 3405-3408.

WALSH, J.B., & RICE, J.R., (1979). Local changes in gravity resulting from deformation, *J. Geoph. Res.,* 84, 165-170.

WILLIAMS, C.A. and WADGE, G. (1998): The effects of topography on magma chamber deformation models: Application to Mt. Etna and radar interferometry, *Geophys. Res. Lett.,* 25, 1549-1552.

WILLIAMS, C.A. and WADGE, G. (2000): An accurate and efficient method for including the effects of topography in three-dimensional elastic models of ground deformation with applications to radar interferometry, *J. Geophys. Res.,* 105(B4), doi: 10.1029/1999JB900307. issn: 0148-0227.

YAMAZAKI, A. and T. SAKAI (2006): Piezomagnetic field associated with the Mogi model considering topographic effects, (in Japanese with English abstract), *Papers in Meteorology and Geophysics,* 57, 21-36.

YANG X. and DAVIS P.M. (1986): Deformation due to a rectangular tension crack in an elastic half-space, *Bull. Seismol. Soc. Am*., 76, 865-881.

YANG, X.-M., P. DAVIS, AND J. H. DIETERICH (1988): Deformation from inflation of a dipping finite prolate spheroid in an elastic half-space as a model for volcanic stressing. *J,. Geophys. Res*.,93, 4249-5257, 1988.

YANG X., DAVIS P.M., DELANEY P.T. and OKUMARA A.T. (1992): Geodetic analysis of dike intrusion and motion of the magma reservoir beneath the summit of Kilauea volcano, Hawaii, 1970-1985, *J. Geophys. Res.,* 97, 3305-3324.

ZIEMIANSKI L. (2003): Hybrid neural network/finite element modelling of wave propagation in infinite domains, *Computers and Structures* 81, 1099–1109, 2003.

ZLOTNICKI, J. and CORNET, F.H. (1986): A numerical model of earthquake-induced piezomagnetic anomalies. *J. Geophys. Res.,* 91 (B1), 709-718.

ZLOTNICKI J., AND LE MOUEL J.L., (1988): Volcanomagnetic effects observed on Piton de la Fournaise Volcano (Reunion Island): 1985-1987, *J. Geophys. Res.,* 93, 9157-9171.

ZURADA, J. M. (1999): *Introduction to Artificial Neural Systems*, PWS Publishing, Boston, Massachusetts.